Kinetically controlled composition of III-V ternary nanostructures

Vladimir G. Dubrovskii[1,*] and Egor D. Leshchenko[2]
[1]Faculty of Physics, St. Petersburg State University, Universitetskaya Embankment 13B, 199034 St. Petersburg, Russia
[2]Submicron Heterostructures for Microelectronics, Research and Engineering Center RAS, Politekhnicheskaya Street, 26, 194021, St. Petersburg, Russia

(Received 25 January 2023; revised 19 March 2023; accepted 1 May 2023; published 22 May 2023)

Controlling the composition of ternary III-V and III-nitride nanomaterials such as vertical nanowires, horizontal nanowires, nanosheets, and nanomembranes grown by different epitaxy techniques is essential for band gap engineering and fabrication of nanoheterostructures with tunable properties. Herein, we investigate the diffusion-induced growth process of III-V ternary materials in different geometries including planar layers, nanomembranes, and horizontal and vertical nanowires grown by selective area epitaxy or with a catalyst droplet on top and derive a rather general equation connecting the composition of ternary solid with the composition of vapor. The form of this vapor-solid distribution remains identical for a wide range of geometries, while the coefficients entering the equation contain thermodynamic factors, kinetic constants of the material transport, and geometrical parameters of the growth template. General properties of the vapor-solid distribution are investigated with respect to material constants, growth condition, and geometry, including the interplay of thermodynamics and growth kinetics leading to the suppression of the miscibility gaps in InGaAs and InGaN systems. A good correlation of the model with the data on the compositions of InGaAs, InGaP, and AlGaAs materials grown by different methods is demonstrated. Overall, these results give a simple analytical tool for understanding the compositional trends and compositional tuning of III-V ternary nanostructures, which should work equally well for Si-Ge and II-VI material systems.

DOI: 10.1103/PhysRevMaterials.7.056001

I. INTRODUCTION

Epitaxial growth of ternary III-V and III-nitride semiconductor alloys and heterostructures based on such alloys has been studied in great detail over the decades [1–8]. The band gap tunability of these materials requires precise control over the composition of ternary III-V alloys and heterointerface abruptness in a wide range of compositions. This is not always possible in planar layers due to the lattice mismatch constrains and the related miscibility gaps at the growth temperatures in III-V ternaries with strong interactions between dissimilar III-V pairs, such as InGaAs and InGaN [9–11]. The growth modeling of III-V ternaries [4–11] has led to vapor-solid distributions which relate the fraction x of an AD binary in a ternary $A_xB_{1-x}D = (AD)_x(BD)_{1-x}$ material (for example, $In_xGa_{1-x}As$) to the A content in vapor, $z = I_A/(I_A + I_B)$, with I_A and I_B as the vapor fluxes of A and B atoms or precursors containing these atoms (for example, In and Ga atoms). The shape of the vapor-solid distribution $x(z)$ depends on the binary interaction constant between AD and BD pairs in a solid in thermal units, thermodynamic parameters related to the chemical potentials of pure elements, and the kinetic parameters describing the growth of AD and BD binaries. The latter are determined by the growth conditions in a given epitaxy technique and on the diffusivity of A, B, and D adatoms on a given substrate surface. These factors can enter the vapor-solid distribution in the form of temperature-dependent equilibrium constants for different chemical reactions at the surface, desorption times, and the effective diffusion lengths of A, B, and D adatoms [5–8].

Ternary III-V nanomaterials of different shapes, including nanoislands, nanowires, and nanomembranes of different orientations with respect to the substrate surface enable a wider tunability of compositions [12,13], which is partly explained by a more efficient relaxation of elastic stress induced by lattice mismatch. Very importantly, high-aspect-ratio III-V nanostructures such as vertical nanowires can be grown on Si substrates without misfit dislocations [12,13]. Hybrid III-V nanoheterostructures on Si substrates can pave the way for monolithic integration of III-V-based photonics with the Si electronic platform. Freestanding ternary III-V and III-nitride nanowires and heterostructures of different types (axial, core-shell, or hybrid nanoheterostructures such as quantum dots in a nanowire) have attracted particular attention in this respect [14–29]. These nanowires can be fabricated by different methods, either via the catalyst-assisted vapor-liquid-solid (VLS) growth mode (with either Au [16,18–20,25] or a group-III [14,23,24] droplet on the nanowire top) or in the catalyst-free selective area epitaxy (SAE) [17,21,22,27]. The growth techniques include molecular beam epitaxy (MBE) [14,17,20,22–24], metalorganic vapor phase epitaxy (MOVPE) [16,18,19,21,25], and hydride vapor phase epitaxy (HVPE) with chloride precursors for group-III elements [26,27]. Compositional modeling of ternary III-V nanowires, as well as III-V nanostructures in general, is much

*dubrovskii@mail.ioffe.ru

 ©2023 American Physical Society

more complex than of planar layers of the same materials. The complexity arises due to the many kinetic pathways for the material transport into a nanostructure through different surfaces or interfaces and the geometrical constrains determined by a particular growth template (droplet diameter, nanowire length, opening size and pitch, nanomembrane height, and so on). On the other hand, this complexity provides more tuning knobs for the compositional variability.

The VLS growth of ternary III-V nanowires is the most complex case for compositional modeling [19,24–26,30–40]. This is explained by the presence of a liquid droplet from which the nanowire monolayers nucleate, with different mechanisms of material transport into the droplet (direct impingement of group-III and V species from vapor, their desorption from the droplet, and diffusion fluxes of group-III adatoms from the substrate surface and nanowire sidewalls) and complex interactions of different atoms in liquid. For an Au-catalyzed ternary $A_xB_{1-x}D$ nanowire, a quaternary A-B-D-Au alloy in the droplet resting on the nanowire top is characterized by the three atomic concentrations c_A, c_B, and c_D of elements A, B, and D, respectively, with the Au concentration $c_{\mathrm{Au}} = 1 - c_A - c_B - c_D$. The A content in liquid is defined according to $y = c_A/(c_A + c_B) = c_A/c_{\mathrm{tot}}$, where c_{tot} is the total concentration of A and B atoms dissolved in liquid. Four types of models are used to find the liquid-solid distribution $x(y)$: (i) the irreversible growth model which, strictly speaking, applies for infinitely large supersaturations of the liquid phase with respect to solid [19,31,38], (ii) the nucleation limited model which assumes that the solid composition is determined in the short nucleation step of the critical island (often consisting of only a few III-V pairs) [31–34,36], (iii) the equilibrium model which assumes the equilibrium state for AD and BD binaries in liquid and solid [24,36], and (iv) the kinetic model which is based on the growth equations for AD and BD binary islands whose size is much larger than the critical size [26,35,37,38,40]. Only the kinetic approach (iv) allows one to consider the interplay of thermodynamic and kinetic factors influencing the nanowire composition.

The most general form of the kinetically controlled liquid-solid distribution is given by [40]

$$y = \frac{x}{k + (1-k)x}(1 + (1-x)\{ka \exp[-f_A(y) - f_D(y)] \times \exp[\omega(1-x)^2] - b\exp[-f_B(y) - f_D(y)]\exp(\omega x^2)\}), \quad (1)$$

with

$$a = \frac{1}{c_D c_{\mathrm{tot}}}\exp\left(\frac{\mu^0_{AD} - \mu^0_A - \mu^0_D}{k_B T}\right),$$
$$b = \frac{1}{c_D c_{\mathrm{tot}}}\exp\left(\frac{\mu^0_{BD} - \mu^0_B - \mu^0_D}{k_B T}\right). \quad (2)$$

Here, $\omega = W/(k_B T)$ is the binary interaction constant of AD and BD pairs in a solid in thermal units, with T as the absolute temperature and k_B as the Boltzmann constant; $\mu^0_{AD} - \mu^0_A - \mu^0_D$ and $\mu^0_{BD} - \mu^0_B - \mu^0_D$ are the chemical potential differences per AD and BD pair in solid binaries (μ^0_{AD} and μ^0_{BD}), and pure liquids ($\mu^0_A + \mu^0_D$ and $\mu^0_B + \mu^0_D$); $f_A(y)$, $f_B(y)$, and $f_D(y)$ are the interaction terms in the chemical potentials of A, B, and D atoms in liquid (defined as $\mu^l_i = \mu^0_i + k_B T \ln c_i + k_B T f_i$ for $i = A$, B, and D), and k is a kinetic constant. Although this expression and its simplified forms have been successfully used for modeling the compositions of different III-V nanowires [26,35,37,38,40], Eq. (1) remains inconsistent in several respects. First, it does not provide the $x(y)$ dependence explicitly due to the presence of the interaction-related y-dependent terms $\exp[-f_A(y) - f_D(y)]$ and $\exp[-f_B(y) - f_D(y)]$ in the right side of Eq. (1). Second, it relates the solid composition to the A content in liquid y rather than the vapor composition z. The $y(z)$ dependence is not known without considering the material transport of A, B, and D atoms into the droplet by different kinetic pathways. Therefore, the vapor-solid distribution $x(z)$ is unknown. Third, for $A_xB_{1-x}D$ ternaries based on the group-III intermix, such as $\mathrm{In}_x\mathrm{Ga}_{1-x}\mathrm{As}$, $\mathrm{Al}_x\mathrm{Ga}_{1-x}\mathrm{As}$, $\mathrm{In}_x\mathrm{Ga}_{1-x}\mathrm{P}$, or $\mathrm{In}_x\mathrm{Ga}_{1-x}\mathrm{N}$, c_D stands for the atomic concentration of highly volatile group-V elements As, P, or N, whose low content in the catalyst droplets (on the order of 0.01 or even less) is usually below the detection limit of any characterization technique [41]. Therefore, c_D is the unknown parameter which very significantly influences the liquid-solid distribution given by Eqs. (1) and (2) (note that the functions $f_i(y)$ depend parametrically on c_D [34,40]). Fourth, the kinetic constant k is generally unknown [40], while its varying in the plausible range may change the solid composition by an order of magnitude.

Consequently, here, we develop a fully self-consistent theory of the diffusion-induced epitaxial growth and the kinetically limited vapor-solid distributions of ternary III-V materials. Compared with earlier works which focus on the kinetically limited composition of ternary III-V VLS nanowires [35,37,39,40], we obtain the explicit form of the vapor-solid distributions for III-V ternaries based on group-III intermix under group-V-rich conditions and demonstrate its generality in a wide range of geometries and growth conditions. Special emphasis is put on the choice of the boundary condition at the growth interface which directly accounts for stoichiometry of a III-V ternary solid. Different geometries are considered, including an echelon of monoatomic steps with a given separation (in planar geometry or on the sidewalls of vertical nanowire), two-dimensional (2D) surface island, horizontal nanowire in one-dimensional (1D) slit in a mask layer, 2D nanomembrane, and vertical nanowire grown by the SAE or VLS method. The diffusion fluxes of A and B atoms are obtained from the two stationary diffusion equations with the appropriate boundary conditions set by the system geometry. It will be shown that the general form of the vapor-solid distribution remains identical for all the systems considered, with coefficients containing geometrical parameters of the structure (separation of monoatomic steps, island radius, width and height of a nanomembrane, nanowire radius and length, and pitch of regular arrays of 1D or 2D openings in a mask layer). The general form of the distribution is like Eq. (1). However, it describes the vapor-solid distribution $x(z)$ for a wide class of ternary III-V nanomaterials rather than the liquid-solid distribution $x(y)$ for VLS III-V nanowires, with a minimum number of parameters. The vapor-solid distribution depends on the well-tabulated binary interaction constant in a solid, temperature-dependent chemical potentials of pure liquids and binary solids, kinetic constants entering the diffusion equations, and geometry of the structure. We analyze the

general properties of the vapor-solid distribution in different growth regimes, its equilibrium solution, and the dependence of the composition of III-V ternaries on the growth conditions and nanostructure geometry. The distribution fits the data on the composition of InGaAs layers and InGaAs and AlGaAs nanowires obtained by different epitaxy techniques in the VLS or SAE regimes quite well.

The paper is organized as follows. In Sec. II, we analyze the general equation for the diffusion flux feeding an echelon of steps of a III-V binary layer and the conditions determining which of the two elements limits the growth process. In the next sections, we concentrate on ternary III-V nanomaterials based on the group-III intermix, growing under group-V-rich conditions. In Sec. III, we discuss the appropriate boundary conditions for the diffusion fluxes of the two elements at the growth interface. In Sec. IV, different geometries of a growing ternary III-V structure are considered, leading to the same form of the diffusion fluxes with modified parameters. In Sec. V, we derive a kinetically limited vapor-solid distribution and analyze its general properties. Section VI deals with some specific features of technologically important InGaAs and InGaP material systems. In Sec. VII, the model is used to fit the experimental data on the composition of InGaAs, InGaP, and AlGaAs ternaries in different growth techniques and template geometries.

II. GROUP-III AND V LIMITED GROWTH REGIMES

To establish a criterion for the group-III or V limited diffusion-induced growth, we consider a III-V binary echelon of steps with separation P, growing on a substrate from the atomic fluxes of group-III and V elements, J_3 and J_5, respectively. The system of stationary diffusion equations describing the coordinate-dependent surface concentrations of group-III and V adatoms, n_3 and n_5, respectively, is given by

$$D_3\frac{d^2n_3}{d\xi^2}+J_3-\frac{n_3}{\tau_3}=0, \quad (3)$$

$$D_5\frac{d^2n_5}{d\xi^2}+J_5-2D_5n_5^2=0, \quad (4)$$

with ξ as the 1D coordinate across the growth front. Here, D_3 and D_5 are the diffusion coefficients of group-III and V adatoms, and τ_3 is the characteristic desorption time of group-III adatoms. In Eq. (4), we consider that group-V elements such as As, P, or N desorb in the form of dimers, at least in the case of MBE [41–44]. Assuming that spatial inhomogeneity of the group-V adatom concentration is small due to their high volatility, Eq. (4) can be linearized around the spatially uniform solution:

$$n_5^0=\sqrt{\frac{J_5}{2D_5}}. \quad (5)$$

The linearized equation for group-V adatoms has the form:

$$D_5\frac{d^2n_5}{d\xi^2}+2J_5-\sqrt{8J_5D_5}n_5=0. \quad (6)$$

By symmetry, the first two boundary conditions for n_3 and n_5 between the steps are given by

$$\left(\frac{dn_3}{d\xi}\right)_{\xi=P/2}=\left(\frac{dn_5}{d\xi}\right)_{\xi=P/2}=0. \quad (7)$$

To ensure that III-V alloy is stoichiometric, both diffusion fluxes into the step must equal each other:

$$j=2D_3\left(\frac{dn_3}{d\xi}\right)_{\xi=0}=2D_5\left(\frac{dn_5}{d\xi}\right)_{\xi=0}. \quad (8)$$

Finally, the chemical potential per III-V pair of adatoms should equal the chemical potential of a III-V binary solid. For the perfect 2D vapor of noninteracting adatoms, this condition is given by

$$n_3(\xi=0)n_5(\xi=0)=n_3^{eq}n_5^{eq}, \quad (9)$$

where $n_3^{eq}n_5^{eq}$ is the product of the two adatom concentrations at which 2D vapor of adatoms is at equilibrium with solid. This $n_3^{eq}n_5^{eq}$ can be related to the chemical potential of pure group-III and V liquids, as will be discussed shortly.

The solution for the diffusion flux, which determines the growth rate of the 2D layer, is readily obtained in the form:

$$j=\frac{(j_3+j_5)}{2\varphi}\left[1-\sqrt{1-\frac{4\varphi}{(1+j_3/j_5)(1+j_5/j_3)}}\right]. \quad (10)$$

Here,

$$\varphi=1-\frac{n_3^{eq}n_5^{eq}}{J_3\tau_3\sqrt{J_5/2D_5}}=1-\frac{n_3^{eq}n_5^{eq}}{J_3\tau_3n_5^0} \quad (11)$$

is proportional to supersaturation of 2D vapor of adatoms with respect to the solid state. The growth rate of a solid III-V binary is positive when $\varphi>0$. The parameters:

$$j_3=2\lambda_3\tanh\left(\frac{P}{2\lambda_3}\right)J_3\varphi,$$
$$j_5=2\left(\frac{2D_5}{J_5}\right)^{1/4}\tanh\left[\frac{P}{(2D_5/J_5)^{1/4}}\right]J_5\varphi, \quad (12)$$

correspond to the group-III and V diffusion fluxes in the group-V and III limited regimes, respectively, with $\lambda_3=\sqrt{D_3\tau_3}$ as the desorption-limited diffusion length of group-III adatoms. From Eq. (12), we have

$$\frac{j_3}{j_5}=\frac{\lambda_3\tanh(P/2\lambda_3)}{(2D_5/J_5)^{1/4}\tanh[P/(2D_5/J_5)^{1/4}]}\frac{J_3}{J_5},$$
$$\frac{j_3}{j_5}\to\frac{\lambda_3J_3}{(2D_5)^{1/4}J_5^{3/4}}\ \text{at}\ P\to\infty,\quad \frac{j_3}{j_5}\to\frac{J_3}{2J_5}\ \text{at}\ P\to 0. \quad (13)$$

Therefore, the j_3/j_5 ratio is reduced to the III/V flux ratio $J_3/2J_5$ for a dense echelon of steps whose separation is much smaller than the diffusion length of group-V adatoms.

From Eq. (10), it follows that $j\to j_3$ at $j_3/j_5\to 0$. Therefore, the growth is group-III limited and given by Eq. (12) for j_3 when $j_3/j_5\ll 1$. In this case, the group-V dependence of the growth rate remains only in supersaturation φ, which is affected by the spatially uniform concentration of group-V adatoms defined in Eq. (5). The growth rate is determined

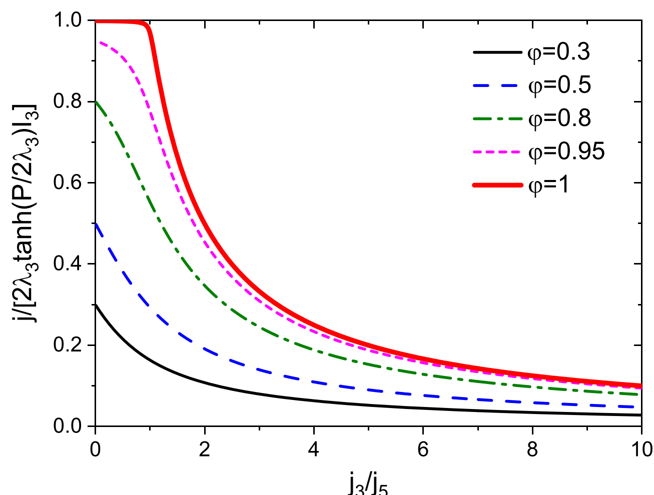

FIG. 1. Diffusion flux j, normalized to its maximum value $2\lambda_3\tanh(P/2\lambda_3)J_3$, as a function of j_3/j_5 for different φ shown in the legend. The bold curve corresponds to the growth at the maximum $\varphi = 1$.

by the diffusion flux of group-III adatoms, while the concentration of group-V adatoms is given by the balance of adsorption and desorption given by Eq. (4) at $D_5 d^2 n_5/d\xi^2 \to 0$. This is the usual assumption used in modeling of the diffusion-induced epitaxial growth of planar III layers and different III-V nanostructures [42,44–50]. The axial growth rate of Au-catalyzed VLS III-V nanowires is usually assumed limited by the direct impingement of group-III atoms from vapor and the diffusion transport of group-III adatoms, including their diffusion from the substrate surface and nanowire sidewalls to the droplet [45–49]. The axial growth rate of SAE III-V nanowires is also thought to be controlled by the group-III diffusion flux [50]. When the growth catalyst of VLS nanowires is replaced by Ga, the Ga droplet resting on the nanowire serves as a reservoir of Ga atoms. As a result, the axial nanowire growth rate becomes limited by the direct impingement and desorption of group-V species [51]. On the other hand, the size of a group-III droplet in the self-catalyzed VLS growth of III-V nanowires is nonstationary. The droplet can either swell or shrink depending on the III/V flux ratio and surface diffusion of group-III adatoms [52,53]. Hence, the growth kinetics of self-catalyzed III-V nanowires and the stable nanowire radius [52,53] generally depend on the surface diffusion flux. The radial growth of VLS [48] and SAE [50] III-V nanowires can also be affected by the group-V flux and the diffusivity of group-V adatoms. This explains the importance of the criterion given by Eq. (13) in modeling the surface diffusion process on the sidewalls of III-V nanowires, where the diffusivity of group-V adatoms may not be negligible [54].

Under group-III-rich conditions, corresponding to $j \to j_5$ at $j_3/j_5 \to \infty$, the growth process is fully controlled by the kinetics of group-V adatoms, as given by Eq. (12) for j_5. The group-III flux dependence of the growth rate remains only in supersaturation φ, which is influenced by the spatially uniform concentration of group-III adatoms $J_3\,\tau_3$ according to Eq. (11). Figure 1 shows the diffusion flux j, normalized to its maximum value $2\lambda_3\tanh(P/2\lambda_3)J_3$ in the group-III limited regime of the diffusion-induced growth of the echelon of steps at $\varphi = 1$. At large $P \gg 2\lambda_3$, this maximum flux equals $2\lambda_3 I_3$, meaning simply that group-III atoms arriving from vapor are collected from the length $2\lambda_3$ of the substrate surface or nanowire side facets, with the coefficient 2 accounting for the two identical fluxes from both sides of the step. Quite obviously, the group-III limited diffusion flux decreases for lower φ. At a given φ, the total diffusion flux of III-V pairs into the step decreases toward larger j_3/j_5 ratios. At large enough j_3/j_5, the diffusion flux saturates at j_5, which is smaller than j_3 and proportional to φ.

III. BOUNDARY CONDITIONS AT THE GROWTH INTERFACE

In the following, we concentrate on the $A_xB_{1-x}D$ ternary materials based on the group-III intermix, which grow by surface diffusion of A and B adatoms under group-V limited conditions as described above. According to the analysis of Sec. II, the surface concentration of group-V adatoms D in this case can be assumed spatially uniform $n_D = n_5^0$. Chemical potentials of AD and BD pairs in a solid are considered using the regular solution model [32,34,36–41]:

$$\mu_{AD}^s = \mu_{AD}^0 + k_BT\ln x + W(1-x)^2,$$
$$\mu_{BD}^s = \mu_{BD}^0 + k_BT\ln(1-x) + Wx^2. \quad (14)$$

Although it is not critical, we ignore the higher-order interactions in a solid [34]. In this case, the binary interaction constant of AD and BD pairs in solid W is independent on composition x. Chemical potentials per $A-D$ and $B-D$ pair in a noninteracting 2D vapor of adatoms can be defined as [44]

$$\mu_{AD}^a = \mu_{AD}^0 + k_BT\ln\left(\frac{n_An_D}{n_A^{eq}n_D^{eq}}\right),$$
$$\mu_{BD}^a = \mu_{BD}^0 + k_BT\ln\left(\frac{n_Bn_D}{n_B^{eq}n_D^{eq}}\right). \quad (15)$$

Here, $n_A^{eq}n_D^{eq}$ and $n_B^{eq}n_D^{eq}$ are the products of A and D (B and D) adatom surface concentrations corresponding to equilibrium of these adatoms with binary solids AD and BD.

The quantities $n_A^{eq}n_D^{eq}$ and $n_B^{eq}n_D^{eq}$ can be related to the chemical potentials of pure liquids μ_A^0, μ_B^0, and μ_D^0 according to [55]

$$\mu_i^a = \mu_i^l + k_BT\ln\theta_i, \quad \mu_D^a = \mu_D^l + k_BT\ln\theta_D, \quad (16)$$

for $i = A,\ B$. Here, $\theta_i = \Omega_i^{2/3}n_i$, $\theta_D = \Omega_D^{2/3}n_D$ as the surface coverages of $i = A,\ B$, and D adatoms and Ω_i, Ω_D as the elementary volumes in pure $i = A$, B, and D liquids. Therefore, for pairs of $A-D$ and $B-D$ adatoms, chemical potentials equal

$$\mu_{AD}^a = \mu_A^0 + \mu_D^0 + k_BT\ln\left(\Omega_A^{2/3}\Omega_D^{2/3}n_An_D\right),$$
$$\mu_{BD}^a = \mu_B^0 + \mu_D^0 + k_BT\ln\left(\Omega_B^{2/3}\Omega_D^{2/3}n_Bn_D\right). \quad (17)$$

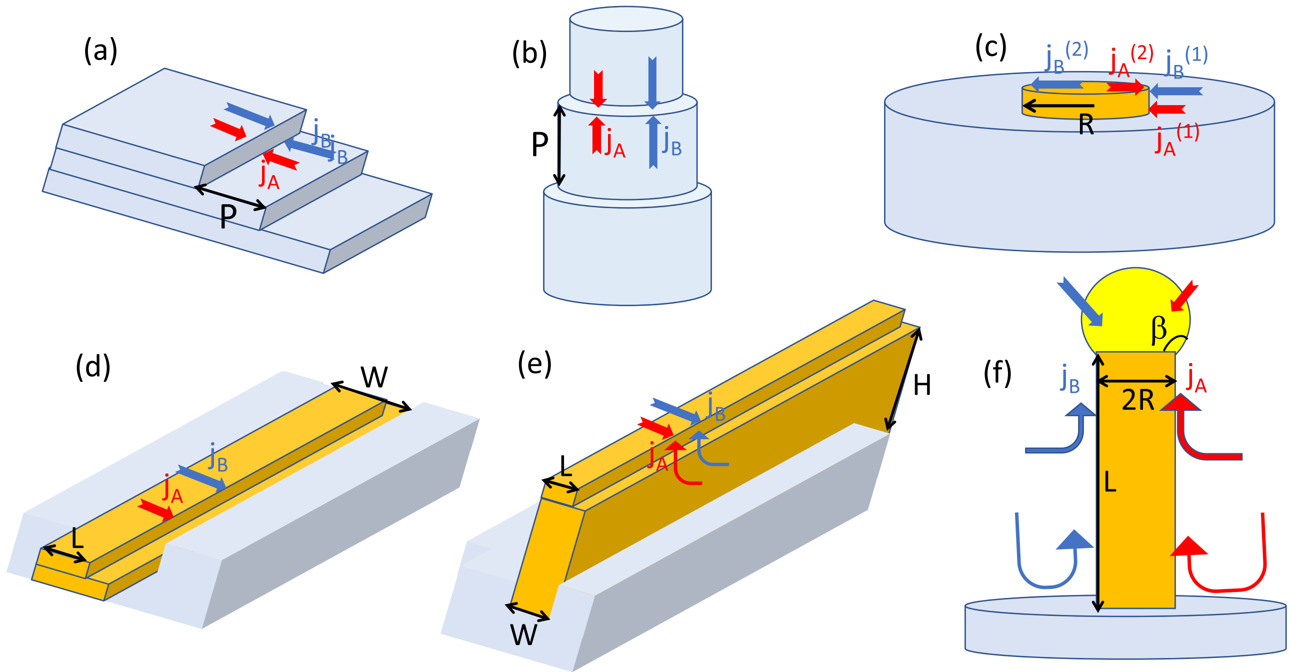

FIG. 2. Different geometries of III-V ternary materials used for calculations of the diffusion fluxes j_A and j_B: echelons of steps with separation P on (a) flat substrate and (b) sidewalls of vertical nanowire; (c) single two-dimensional (2D) island on flat substrate; (d) horizontal nanowire in infinitely long one-dimensional (1D) slit of width W, with L as the step width; (e) nanomembrane of height H in infinitely long 1D slit of width W; (f) vertical vapor-liquid-solid (VLS) nanowire of radius R and length L, with a liquid catalyst droplet resting on its top with a constant angle β. The same nanowire without droplet corresponds to the catalyst-free selective area epitaxy (SAE) regime of nanowire growth.

Comparing it with Eq. (15), we find

$$n_A^{\rm eq}n_D^{\rm eq}=\frac{1}{\Omega_A^{2/3}\Omega_D^{2/3}}\exp\left(\frac{\mu_{AD}^0-\mu_A^0-\mu_D^0}{k_BT}\right),$$
$$n_B^{\rm eq}n_D^{\rm eq}=\frac{1}{\Omega_B^{2/3}\Omega_D^{2/3}}\exp\left(\frac{\mu_{BD}^0-\mu_B^0-\mu_D^0}{k_BT}\right). \quad (18)$$

The boundary conditions for A and B adatoms at the growth interface (the step edge) of any shape (at $\xi=0$) are given by $\mu_{AD}^a(\xi=0)=\mu_{AD}^s$ and $\mu_{BD}^a(\xi=0)=\mu_{BD}^s$. Using Eqs. (14) and (15), we get

$$n_A(\xi=0)=n_A^*=\frac{n_A^{\rm eq}n_D^{\rm eq}}{n_D}x\exp[\omega(1-x)^2],$$
$$n_B(\xi=0)=n_B^*=\frac{n_B^{\rm eq}n_D^{\rm eq}}{n_D}(1-x)\exp(\omega x^2), \quad (19)$$

Here, $\omega=W/(k_BT)$ is the binary interaction constant in thermal units, as in Eq. (1). The quantities $n_A^{\rm eq}n_D^{\rm eq}$ and $n_B^{\rm eq}n_D^{\rm eq}$ are defined in Eq. (18) through the chemical potentials of pure elements. The surface concentration of group-V adatoms n_D is given by Eq. (5). Therefore, these boundary conditions contain no unknown parameters. For a binary III-V material with $x=1$, Eq. (19) for $n_A(\xi=0)$ is equivalent to Eq. (9) under group-V-rich growth conditions. The curvature effects such as the Gibbs-Thomson effect of elevation of chemical potential in small islands or nanowires [41] can be included directly in these n_A^* and n_B^*.

IV. GROWTH OF III-V TERNARIES IN DIFFERENT GEOMETRIES

Figure 2 shows the geometries considered for calculation of the diffusion fluxes of group-III adatoms A and B, denoted j_A and j_B, respectively. The two stationary diffusion equations for surface concentrations of group-III adatoms A and B have the form like Eq. (3):

$$D_A\frac{d^2n_A}{d\xi^2}+J_A-\frac{n_A}{\tau_A}=0,\quad D_B\frac{d^2n_A}{d\xi^2}+J_B-\frac{n_B}{\tau_B}=0. \quad (20)$$

Here, D_A and D_B denote the diffusion coefficients of A and B adatoms, while τ_A and τ_B are their characteristic desorption times. The corresponding desorption-limited diffusion lengths are given by $\lambda_A=\sqrt{D_A\tau_A}$ and $\lambda_B=\sqrt{D_B\tau_B}$. We plan to calculate the diffusion fluxes of A and B adatoms into the growing step (which determine the solid composition x) as functions of the incoming vapor fluxes (which are related to the vapor composition z), adatom diffusion lengths, desorption times, and geometry of a ternary III-V structure. The two diffusion equations for A and B adatoms require four boundary conditions. The diffusion lengths λ_A, λ_B and desorption times τ_A, τ_B enter the diffusion equations and will remain in the solutions. The two boundary conditions at the adsorbing step edge are given by the thermodynamic values n_A^* and n_B^*. The other two boundary conditions are determined by geometry, as will be discussed in detail for each structure shown in Fig. 2.

For an echelon of steps with separation P growing on a flat surface or sidewalls of vertical nanowire, as shown in Figs. 2(a) and 2(b), the boundary conditions at the step are

given by

$$n_A(\xi = 0) = n_A^*, \quad n_B(\xi = 0) = n_B^*, \tag{21}$$

with the composition-dependent n_A^* and n_B^* given by Eq. (19). By symmetry, the two boundary conditions between the steps are like Eq. (7):

$$\left(\frac{dn_A}{d\xi}\right)_{\xi=P/2} = 0, \quad \left(\frac{dn_B}{d\xi}\right)_{\xi=P/2} = 0. \tag{22}$$

The solutions for the diffusion fluxes:

$$j_A = D_A\left(\frac{dn_A}{d\xi}\right)_{\xi=0}, \quad j_B = D_B\left(\frac{dn_B}{d\xi}\right)_{\xi=0}, \tag{23}$$

are obtained in the form:

$$j_A = \Lambda_A\left(J_A - \frac{n_A^*}{\tau_A}\right), \quad \Lambda_A = \lambda_A \tanh\left(\frac{P}{2\lambda_A}\right),$$
$$j_B = \Lambda_B\left(J_B - \frac{n_B^*}{\tau_B}\right), \quad \Lambda_B = \lambda_B \tanh\left(\frac{P}{2\lambda_B}\right). \tag{24}$$

Here and below, we do not write an unimportant coefficient 2 in the diffusion fluxes, as it cancels out the ratio j_A/j_B which determines the solid composition x. These solutions are like the classical expressions for the diffusion flux of adatoms in the one-component deposition process [55,56], with Λ as the pitch-dependent effective diffusion length which accounts for the competition of the neighboring steps for the adatom diffusion flux.

At large enough pitches such that $P \gg 2\lambda_i$ for i = A, B, these solutions describe the growth of a single monoatomic step with the diffusion fluxes given by

$$j_A = \lambda_A\left(J_A - \frac{n_A^*}{\tau_A}\right), \quad j_B = \lambda_B\left(J_B - \frac{n_B^*}{\tau_B}\right). \tag{25}$$

In the opposite case of small pitches such that $P \ll 2\lambda_i$ for i = A, B, the solutions become

$$j_A = \frac{P}{2}\left(J_A - \frac{n_A^*}{\tau_A}\right), \quad j_B = \frac{P}{2}\left(J_B - \frac{n_B^*}{\tau_B}\right). \tag{26}$$

The physical meaning of these expressions is quite simple. Group-III adatoms A and B, deposited from the atomic fluxes J_A and J_B, migrate to the growing steps from the effective collection lengths Λ_A and Λ_B and are rejected by the steps with the probability densities n_A^*/τ_A and n_B^*/τ_B. The latter depend on the solid composition x due to the composition-dependent chemical potentials of AD and BD pairs in the ternary solid $A_xB_{1-x}D$. The collection lengths are different due to different λ_A and λ_B for A and B adatoms, as in Eqs. (24) or (25). For very dense echelons of steps, this difference disappears because both types of adatoms are collected from the length $P/2$, as in Eq. (26).

Let us now consider the growth of a single circular 2D island on a flat substrate, as shown in Fig. 2(c). In this case, both A and B adatoms are collected from the substrate surface and island surface. For the adatom surface concentrations on the substrate surface around the island, $n_i(r)$ for $i = A, B$, with r as the distance from the island origin, the stationary 2D diffusion equations have the form:

$$D_i \Delta n_i + J_i - \frac{n_i}{\tau_i} = 0. \tag{27}$$

The boundary conditions are given by

$$n_i(r \to \infty) = J_i\tau_i, \quad n_i(r = R) = n_i^*, \tag{28}$$

corresponding to the balance of the adsorption-desorption processes far away from the island and equilibrium chemical potential at the island periphery of radius R. The solutions for adatom concentrations are obtained in the form:

$$n_i = J_i\tau_i - (J_i\tau_i - n_i^*)\frac{K_0(r/\lambda_i)}{K_0(R/\lambda_i)}, \tag{29}$$

where $K_0(X)$ is the modified Bessel function of the second type of order zero. The diffusion fluxes from the substrate surface to the island periphery,

$$j_i^{(1)} = D_i\left(\frac{dn_i}{dr}\right)_{r=R}, \tag{30}$$

are obtained in the form:

$$j_i^{(1)} = \lambda_i \frac{K_1(R/\lambda_i)}{K_0(R/\lambda_i)}\left(J_i - \frac{n_i^*}{\tau_i}\right), \tag{31}$$

with $K_1(X)$ as the modified Bessel function of the second type of order one.

For the adatom surface concentrations on the island surface, $n_i'(r)$ for $i = A, B$, the stationary 2D diffusion equations are the same as given by Eq. (27). The boundary conditions become

$$\left(\frac{dn_i'}{dr}\right)_{r=0} = 0, \quad n_i'(r = R) = n_i^*, \tag{32}$$

corresponding to zero diffusion flux at the island center. The solutions for adatom concentrations are obtained in the form:

$$n_i' = J_i\tau_i - (J_i\tau_i - n_i^*)\frac{I_0(r/\lambda_i)}{I_0(R/\lambda_i)}, \tag{33}$$

where $I_0(X)$ is the modified Bessel function of the first type of order zero.

The diffusion fluxes $j_i^{(2)}$ are obtained using Eq. (30) for this n_i':

$$j_i^{(2)} = \lambda_i \frac{I_1(R/\lambda_i)}{I_0(R/\lambda_i)}\left(J_i - \frac{n_i^*}{\tau_i}\right),$$

with $I_1(X)$ as the modified Bessel function of the first type of order one. The total fluxes into the island, $j_i = j_i^{(1)} + j_i^{(2)}$ for $i = A, B$ yield the final result for the 2D island in the form:

$$j_A = \Lambda_A\left(J_A - \frac{n_A^*}{\tau_A}\right), \quad \Lambda_A = \lambda_A\left[\frac{K_1(R/\lambda_A)}{K_0(R/\lambda_A)} + \frac{I_1(R/\lambda_A)}{I_0(R/\lambda_A)}\right],$$
$$j_B = \Lambda_B\left(J_B - \frac{n_B^*}{\tau_B}\right), \quad \Lambda_B = \lambda_B\left[\frac{K_1(R/\lambda_B)}{K_0(R/\lambda_B)} + \frac{I_1(R/\lambda_B)}{I_0(R/\lambda_B)}\right]. \tag{34}$$

These fluxes have the same form as Eq. (24) but with diffusion lengths Λ_A and Λ_B which account for the 2D geometry of the growing island.

For a planar nanowire growing in a lithographically patterned, infinitely long 1D slit in a dielectric mask layer (for example, a SiO_x layer [57,58]) which reflects both A and B fluxes (the reflecting mask hereinafter), A and B adatoms can form only on the top surface of the nanowire. Without surface diffusion of adatoms from or onto the mask layer, we need

to consider the two diffusion fluxes originating from A and B atoms landing on the left and right sides of the step edge [see Fig. 2(d)]. For the first population of adatoms, the boundary conditions for the 1D diffusion equation are given by

$$\left(\frac{dn_i}{dy}\right)_{y=L}=0,\quad n_i(y=0)=n_i^*, \tag{35}$$

corresponding to zero flux of adatoms from the mask and equilibrium chemical potential at the edge of the step of width L. The diffusion fluxes of A and B adatoms from the terrace of width L are obtained in the form:

$$j_i^{(1)}=\lambda_i\tanh\left(\frac{L}{\lambda_i}\right)\left(J_i-\frac{n_i^*}{\tau_i}\right). \tag{36}$$

For the second population of adatoms, the boundary conditions modify to

$$\left(\frac{dn_i'}{dy}\right)_{y=W-L}=0,\quad n_i(y=0)=n_i^*, \tag{37}$$

because the width of the second terrace equals $W-L$. The adatom diffusion fluxes from this terrace are given by

$$j_i^{(2)}=\lambda_A\tanh\left(\frac{W-L}{\lambda_i}\right)\left(J_i-\frac{n_i^*}{\tau_i}\right). \tag{38}$$

Averaging these fluxes over the terrace width according to [59]

$$j_i=\frac{1}{W}\int_0^W dL\left[j_i^{(1)}(L)+j_i^{(2)}(L)\right]=\frac{2}{W}\int_0^W dL j_i^{(1)}(L) \tag{39}$$

yields the final result for the diffusion fluxes of A and B adatoms in the form:

$$j_A=\Lambda_A\left(I_A-\frac{n_A^*}{\tau_A}\right),\quad \Lambda_A=\frac{2\lambda_A^2}{W}\ln\left[\cosh\left(\frac{W}{\lambda_A}\right)\right],$$
$$j_B=\Lambda_B\left(I_B-\frac{n_B^*}{\tau_B}\right),\quad \Lambda_B=\frac{2\lambda_B^2}{W}\ln\left[\cosh\left(\frac{W}{\lambda_B}\right)\right]. \tag{40}$$

These expressions are like Eqs. (24) and (34), with the effective diffusion lengths Λ_A and Λ_B accounting for the geometry of the horizontal nanowire with lithographically defined width W.

We now consider the growth of high nanomembranes outside infinitely long 1D slits of width W [57–64], illustrated in Fig. 2(e). If the mask is reflecting, as in the previous case, A and B atoms can land only on the nanomembrane sidewalls and top facet. Here, A and B adatoms can diffuse from the nanomembrane sidewalls to the top facet and contribute to the nanomembrane growth. The diffusion exchange of material between the sidewall and top facets complicates the growth picture compared with the previous cases. Let us first consider the adatom populations on the nanomembrane sidewalls, with surface concentrations n_i^f for $i=A$ and B. The first boundary condition at the nanomembrane-substrate interface corresponds to zero adatom diffusion fluxes from the mask:

$$\left(\frac{dn_i^f}{d\xi}\right)_{\xi=H}=0. \tag{41}$$

Therefore, n_i^f can be presented as

$$n_i^f=J_i\tau_{fi}+a_i\cosh\left(\frac{\xi-H}{\lambda_{fi}}\right), \tag{42}$$

with arbitrary constants a_i. Here, τ_{fi} are the characteristic desorption times of adatoms on the sidewall facets, with the corresponding diffusion lengths $\lambda_{fi}=\sqrt{D_{fi}\tau_{fi}}$. For the adatom surface concentrations on the nanomembrane top, the first boundary condition writes

$$n_i(\eta=0)=n_i^*, \tag{43}$$

yielding

$$n_i=J_i\tau_i-(J_i\tau_i-n_i^*)\cosh\left(\frac{\eta}{\lambda_i}\right)+b_i\sinh\left(\frac{\eta}{\lambda_i}\right), \tag{44}$$

with arbitrary constants b_i. Here, λ_i are the adatom diffusion lengths on the top facet of the nanomembrane, with τ_i as the desorption times of adatoms from the top facet.

To find the constants a_i and b_i, we use the boundary conditions of the transition rate theory [58,59,65,66] at the transparent edge of the nanomembrane (corresponding to $\xi=0$ and $\eta=L$):

$$D_i^f\left(\frac{dn_i^f}{d\xi}\right)_{\xi=0}=D_i\left(\frac{dn_i}{d\eta}\right)_{\eta=L}, \tag{45}$$

$$D_i^f\left(\frac{dn_i^f}{d\xi}\right)_{\xi=0}=k_{fi}^+n_i^f(\xi=0)-k_{fi}^-n_i(\eta=L). \tag{46}$$

Here, $k_{fi}^{\pm}$ denote the transition rate constants for the adatom transfers from the nanomembrane sidewall to the top facet and back. Using Eqs. (42) and (44) in Eqs. (45) and (46) allows us to determine the a_i and b_i values. After that, the adatom diffusion fluxes are readily obtained in the form:

$$j_i^{(1)}=\lambda_i\tanh\left(\frac{L}{\lambda_i}+\varphi_i\right)\left(J_i-\frac{n_i^*}{\tau_i}\right)+\frac{(k_{fi}^+\tau_{fi}-k_{fi}^-\tau_i)}{\zeta_i}\frac{1}{\cosh(L/\lambda_i)+U_i\sinh(L/\lambda_i)}J_i. \tag{47}$$

The functions entering this expression are defined by

$$\zeta_i=1+\frac{k_{fi}^+\tau_{fi}}{\lambda_{fi}}\text{cotanh}\left(\frac{H}{\lambda_{fi}}\right),$$
$$U_i=\frac{k_{fi}^-\tau_i}{\lambda_i\zeta_i},\quad \varphi_i=\text{arctanh}(U_i). \tag{48}$$

The diffusion fluxes defined in Eq. (44) give the contributions of adatoms diffusing from one side of the step edge, where the terrace width equals L. The solution for the second contribution originating from adatoms from another terrace of width $W-L$ is given by Eq. (44) in which L is replaced by $W-L$, as in the previous example for planar nanowire. Taking the average according to Eq. (39), the final result for the diffusion fluxes of A and B adatoms is obtained in the

form:

$$j_A = \tilde{\lambda}_A\left(J_A - \frac{n_A^*}{\tau_A}\right) + l_A J_A,$$
$$j_B = \tilde{\lambda}_B\left(J_B - \frac{n_B^*}{\tau_B}\right) + l_B J_B. \quad (49)$$

Here, the effective diffusion lengths $\tilde{\lambda}_A$, $\tilde{\lambda}_B$ and characteristic collection lengths l_A, l_B are given by

$$\tilde{\lambda}_A = \frac{2\lambda_A^2}{W}\ln\left[\frac{\cosh(W/\lambda_A + \varphi_A)}{\cosh(\varphi_A)}\right],$$
$$\tilde{\lambda}_B = \frac{2\lambda_B^2}{W}\ln\left[\frac{\cosh(W/\lambda_B + \varphi_B)}{\cosh(\varphi_B)}\right], \quad (50)$$

$$l_A = \frac{4\lambda_A(k_{fA}^+\tau_{fA} - k_{fA}^-\tau_A)}{W\zeta_A}\frac{1}{\sqrt{1-U_A^2}} \times \arctan\left[\frac{\sqrt{1-U_A^2}\tanh(W/2\lambda_A)}{1+U_A\tanh(W/2\lambda_A)}\right],$$
$$l_B = \frac{4\lambda_B(k_{fB}^+\tau_{fB} - k_{fB}^-\tau_B)}{W\zeta_B}\frac{1}{\sqrt{1-U_B^2}} \times \arctan\left[\frac{\sqrt{1-U_B^2}\tanh(W/2\lambda_B)}{1+U_B\tanh(W/2\lambda_B)}\right]. \quad (51)$$

The diffusion fluxes feeding the nanomembrane have forms which are different from the previous expressions given by Eqs. (24)–(26), (34), or (40). The difference is in the presence of the source terms l_iJ_i originating from the sidewall adatoms diffusing to the nanowire top across the transparent edges on top of the nanomembrane. These terms describe surface diffusion of group-III adatoms over the transparent edge at the nanomembrane top according to the boundary condition given by Eq. (46). The diffusion flux over the edge is proportional to the difference $\delta_i = k_{fi}^+\tau_{fi} - k_{fi}^-\tau_i$. A similar result is valid for cylindrical nanowires [66].

Diffusion-induced contribution to the axial growth rate of VLS III-V nanowires [45–49], catalyst-free III-V nanowires [50], and GaAs nanomembranes grown by MBE [58] is well known and often exceeds the direct impingement flux by an order of magnitude. On the other hand, the source terms can cancel out under certain conditions. For example, if the sidewall and top facets have close atomic arrangements such that the equilibrium impinging flux J_i^{eq} is the same for both facets, the diffusion flux over the edge cancels out for the following reason. The adatom concentrations on the nanomembrane facets in equilibrium with the vapor phase are given by $n_{fi}^{eq} = J_i^{eq}\tau_{fi}$ and $n_i^{eq} = J_i^{eq}\tau_i$. The net flux of adatoms over the nanomembrane edge can be found by substituting these concentrations into Eq. (46): $k_{fi}^+n_{fi}^{eq} - k_{fi}^-n_{fi}^{eq} = J_i^{eq}\delta_i$. The net flux should be zero in equilibrium, which yields $\delta_i = 0$ and hence zero diffusion flux over the edge at any time. This example shows that the source terms l_iJ_i in Eq. (51) are highly dependent on the type of facets and growth conditions. However, they are not zero in the general case and influence the adatom incorporation kinetics and the resulting composition of solid. The conventional form of the diffusion fluxes is resumed by the renormalization of the desorption times:

$$j_A = \Lambda_A\left(J_A - \frac{n_A^*}{T_A}\right),\quad \Lambda_A = \tilde{\lambda}_A + l_A,\quad T_A = \frac{(\tilde{\lambda}_A + l_A)}{\tilde{\lambda}_A}\tau_A,$$
$$j_B = \Lambda_B\left(J_B - \frac{n_B^*}{T_B}\right),\quad \Lambda_B = \tilde{\lambda}_B + l_B,\quad T_B = \frac{(\tilde{\lambda}_B + l_B)}{\tilde{\lambda}_B}\tau_B. \quad (52)$$

These expressions have the same form as Eqs. (24)–(26), (34), and (40). However, for the first time in our examples, the characteristic times T_A and T_B are different from the desorption times and contain geometrical parameters of the nanostructure W and H.

Recent results of Ref. [58] strongly suggest that SAE of GaAs nanomembranes on patterned SiO_2/GaAs(100) substrates by MBE at 630 °C and a V/III flux ratio of 80 is influenced by surface diffusion of Ga adatoms from the nanomembranes onto the mask surface. The observed increase of the nanomembrane growth rate with increasing the slit width and decreasing the pitch can only be explained by such a reverse direction of the Ga diffusion flux [58,59]. A detailed growth model for nanomembrane growth on adsorbing substrates with surface diffusion of group-III adatoms on the mask surface has been developed in Ref. [59]. Using the result of Ref. [59] for A and B adatoms, the diffusion fluxes into the growing step on the nanomembrane top in this case are given by Eq. (52) with

$$\tilde{\lambda}_A = \frac{2\lambda_A^2}{W}\ln\left[\frac{\cosh(W/\lambda_A + \psi_A)}{\cosh(\psi_A)}\right],\quad \tilde{\lambda}_B = \frac{2\lambda_B^2}{W}\ln\left[\frac{\cosh(W/\lambda_B + \psi_B)}{\cosh(\psi_B)}\right], \quad (53)$$

$$l_A = \frac{4\lambda_A}{WF_A}\left[k_{fA}^+\tau_{fA} - k_{fA}^-\tau_A + \frac{k_{fA}^+}{k_{sA}^-}\frac{\gamma_A(k_{sA}^+\tau_{sA} - k_{sA}^-\tau_{fA})}{\sinh(H/\lambda_{fA}) + \gamma_A\cosh(H/\lambda_{fA})}\right]\frac{1}{\sqrt{1-\Gamma_A^2}}\arctan\left[\frac{\sqrt{1-\Gamma_A^2}\tanh(W/2\lambda_A)}{1+\Gamma_A\tanh(W/2\lambda_A)}\right],$$

$$l_B = \frac{4\lambda_B}{WF_B}\left[k_{fB}^+\tau_{fB} - k_{fB}^-\tau_B + \frac{k_{fB}^+}{k_{sB}^-}\frac{\gamma_B(k_{sB}^+\tau_{sB} - k_{sB}^-\tau_{fB})}{\sinh(H/\lambda_{fB}) + \gamma_B\cosh(H/\lambda_{fB})}\right]\frac{1}{\sqrt{1-\Gamma_B^2}}\arctan\left[\frac{\sqrt{1-\Gamma_B^2}\tanh(W/2\lambda_B)}{1+\Gamma_B\tanh(W/2\lambda_B)}\right]. \quad (54)$$

The parameters entering these expressions are given by

$$\Gamma_i = \frac{k_{fi}^- \tau_i}{\lambda_i F_i}, \quad \psi_i = \text{arctanh}(\Gamma_i), \quad \gamma_i = \frac{k_{si}^- \tau_{fi}}{\lambda_{fi}\delta_i},$$
$$\delta_i = 1 + \frac{k_{si}^+ \tau_{si}}{\lambda_{si}} \text{cotanh}\left(\frac{P-W}{2\lambda_{si}}\right),$$
$$F_i = 1 + \frac{k_{fi}^+ \tau_{fi}}{\lambda_{fi}} \left[\frac{1+\gamma_i \tanh(H/\lambda_{fi})}{\gamma_i + \tanh(H/\lambda_{fi})}\right], \tag{55}$$

for $i = A,\ B$.

These expressions are more complex than the previous case of the reflecting mask due to the presence of the two transparent edges on the nanomembrane top and at the nanomembrane-mask interface. Consequently, the adatom diffusion fluxes depend on the three diffusion lengths λ_i, λ_{fi}, and λ_{si} corresponding to adatoms on the top facet, nanomembrane sidewalls, and mask surface, respectively, with τ_i, τ_{fi}, and τ_{si} as the corresponding desorption times. The transition rate constants $k_{fi}^{\pm}$ describe the adatom transfers from the nanomembrane sidewall to the top facet and back, as in the previous case of reflecting mask. The transition rate constants $k_{si}^{\pm}$ describe the adatom transfers from the mask surface to the nanomembrane sidewalls and back. The characteristic times T_A and T_B are again different from the desorption times. The parameters Λ_A, Λ_B, T_A, and T_B depend on the system geometry which include the slit width.

As mentioned above, III-V VLS nanowires are the most complex cases for compositional modeling due to the presence of a liquid catalyst droplet at the growth interface [30–41]. The liquid state in the droplet is characterized by a certain supersaturation with respect to the reference state in a solid, which is the driving force for crystallization at the liquid-solid interface under the droplet [55]. This supersaturation is related to the chemical potential difference $\Delta\mu = \mu_A^l + \mu_D^l - \mu_{AD}^s$ for a binary AD nanowire, with μ_A^l and μ_D^l as the chemical potentials of A and D atoms in liquid [41,67]. As known from the growth theory of binary III-V nanowires, the VLS growth rate can be limited by either the material transport, including the diffusion transport of group-III adatoms from the substrate surface and nanowire sidewalls to the droplet [45–49,52,53,55], or by nucleation of III-V islands at the liquid-solid interface [41,51,66,68–70]. In the general case, the liquid supersaturation should be obtained in the self-consistent manner by equalizing the Zeldovich nucleation rate on a given surface area with the total material flux into the droplet [41,51,66]. Otherwise, the liquid chemical potential remains as an external parameter of the growth equations which determines particularly the so-called negative diffusion flux of group-III atoms from the droplet to the nanowire sidewalls [49,71]. In the case of a VLS $A_xB_{1-x}D$ ternary nanowire, one needs to consider the chemical potential differences for AD and BD pairs, $\Delta\mu_{AD}(x, y, c_{\text{tot}}, c_D) = \mu_A^l(y, c_{\text{tot}}, c_D) + \mu_D^l(y, c_{\text{tot}}, c_D) - \mu_{AD}^s(x)$ and $\Delta\mu_{BD}(x, y, c_{\text{tot}}, c_D) = \mu_B^l(y, c_{\text{tot}}, c_D) + \mu_D^l(y, c_{\text{tot}}, c_D) - \mu_{BD}^s(x)$ [32–34,36–40], which depend on the four variables x, y, c_{tot}, and c_D in the Au-catalyzed VLS growth.

The most general form of the transport equation for the normalized axial growth rates dL_i/dt describing the incorporation of AD and BD pairs into a VLS III-V ternary nanowire is given by [41]

$$g_i = \frac{1}{\Omega_{35}} \frac{dL_i}{dt} = g_i^+ - g_i^-, \tag{56}$$

for $i = A, B$, with Ω_{35} as the elementary volume per III-V pair in a solid and

$$g_i^+ = \left[\chi_i^+ + \frac{\lambda_{fi}}{R} + \left(\frac{\lambda_{si}}{R}\right)^2\right] J_i. \tag{57}$$

These g_i^+ describe the group-III atomic fluxes entering the droplet resting on top of a nanowire of radius R via different kinetic pathways. The first χ_i^+ terms stand for the direct impingement and depend on the beam angle θ_i with respect to the substrate normal and the droplet contact angle β according to Ref. [72]. In MOVPE and HVPE growths, we simply have $\chi_i^+ = 2/(1 + \cos\beta)$ for both direct fluxes. The second λ_{fi}/R terms give the diffusion flux of sidewall adatoms, while the third $(\lambda_{si}/R)^2$ terms describe the diffusion flux of adatoms from the substrate surface. The characteristic diffusion lengths λ_{fi} and λ_{si} are constant only in the simplest approximation [41,55], while generally they may depend on the nanowire length L, radius R, and separation between the nanowires P. The corresponding expressions can be found, for example, in Refs. [41,49,55,66,69]. All these contributions are proportional to the vapor fluxes J_i according to Eq. (57).

The fluxes g_i^- correspond to group-III adatoms leaving the droplet by desorption and negative diffusion from the droplet onto the nanowire sidewalls and substrate surface [41,49,66,71]. All these fluxes generally depend on the chemical potentials of A and B atoms $\mu_A^l(y, c_{\text{tot}}, c_D)$ and $\mu_B^l(y, c_{\text{tot}}, c_D)$. The results of Refs. [24,36] show, however, that the composition of III-V ternary nanowires can be well described assuming the liquid-solid equilibrium for AD and BD pairs, corresponding to $\Delta\mu_{AD} = \Delta\mu_{BD} = 0$. In this case, the negative fluxes of group-III adatoms leaving the droplet in the transport-limited growth regime can be approximated in the form:

$$g_i^- = \left[\frac{\chi_i^-}{\tau_{li}} + \frac{\lambda_{fi}}{R}\frac{1}{\tau_{fi}} + \left(\frac{\lambda_{si}}{R}\right)^2 \frac{1}{\tau_{si}}\right] n_i^*. \tag{58}$$

Here, $\chi_i^- = 2/(1 + \cos\beta)$ in most cases, whereas τ_{li} are the characteristic desorption times from the droplet surface. These τ_{li} generally depend on the liquid composition y which corresponds to equilibrium with solid having the composition x. However, in many cases, $\tau_{li} \to \infty$ is a good approximation for group-III atoms which do not desorb from the catalyst droplet at a growth temperature [48,55,66,71]. The quantities n_i^*/τ_{fi} and n_i^*/τ_{si} are the diffusion fluxes of A and B adatoms from the droplet onto the nanowire sidewalls and the substrate surface which equalize the direct fluxes J_i under equilibrium conditions. The x-dependent quantities n_i^* are given by Eq. (19) for $i = A, B$. With neglect of desorption from the catalyst droplet, no characteristics of the liquid state remain in Eq. (58) which is entirely determined by the parameters of group-III adatoms on the nanowire sidewalls and substrate surface.

Using Eqs. (57) and (58) in Eq. (56), we obtain the total fluxes of A and B adatoms to the top of the VLS III-V ternary

nanowires in the form:

$$g_A = \bar{\varphi}_A = \bar{\Lambda}_A\left(J_A - \frac{n_A^*}{T_A}\right), \quad g_B = \bar{\varphi}_B = \bar{\Lambda}_B\left(J_B - \frac{n_B^*}{T_B}\right). \tag{59}$$

Here,

$$\bar{\Lambda}_A = \chi_A^+ + \frac{\lambda_{fA}}{R} + \left(\frac{\lambda_{sA}}{R}\right)^2, \quad \bar{\Lambda}_B = \chi_B^+ + \frac{\lambda_{fB}}{R} + \left(\frac{\lambda_{sB}}{R}\right)^2 \tag{60}$$

are the effective normalized diffusion lengths, and

$$T_A = \frac{\chi_A^+ + \lambda_{fA}/R + (\lambda_{sA}/R)^2}{\chi_A^-/\tau_{lA} + (\lambda_{fA}/R)/\tau_{fA} + (\lambda_{sA}/R)^2/\tau_{sA}},$$
$$T_B = \frac{\chi_B^+ + \lambda_{fB}/R + (\lambda_{sB}/R)^2}{\chi_B^-/\tau_{lB} + (\lambda_{fB}/R)/\tau_{fB} + (\lambda_{sB}/R)^2/\tau_{sB}} \tag{61}$$

are the characteristic times determining the negative flux. These fluxes have the same form as Eq. (52), although the dimension of the fluxes is different. Therefore, the kinetically controlled composition of VLS III-V ternary nanowires under the assumption of liquid-solid equilibrium is reduced to the previous model. We note that this model may be insufficient to describe the compositional profiles across axial nanowire heterostructures, influenced by the so-called reservoir effect [23,24,32,36,40]. However, the stationary composition of nanowires under time-independent material fluxes should be resumed. For SAE III-V ternary nanowires without any droplet on top [17,21,22,50], the model given by Eqs. (59) to (61) becomes exact, with $\chi_i^+ = \chi_i^- = 1$ corresponding to the flat top facet and τ_{li} replaced to the adatom desorption times from this facet τ_i.

V. KINETICALLY CONTROLLED VAPOR-SOLID DISTRIBUTION AND ITS GENERAL PROPERTIES

The main result of the previous section can be formulated as follows. For all the systems considered, the diffusion-induced growth of ternary $A_xB_{1-x}D$ nanostructures based on the group-III intermix from vapor fluxes J_A, J_B, and J_D under group-V-rich conditions is driven by the diffusion fluxes of A and B adatoms:

$$j_A = \Lambda_A\left(J_A - \frac{n_A^*}{T_A}\right), \quad j_B = \Lambda_B\left(J_B - \frac{n_B^*}{T_B}\right). \tag{62}$$

The x-dependent equilibrium concentrations n_A^* and n_B^* are given by Eq. (19) in which n_D is related to the group-V flux J_D by Eq. (5). The parameters of the diffusion fluxes Λ_i and T_i contain the geometrical constants of a nanostructure. This form of these fluxes has been demonstrated for a wide range of systems, and we suspect that the result is valid regardless of the particular shape of the structure.

Let us now consider the vapor-solid distribution following from Eq. (62). Clearly, the AD fraction in ternary solid $A_xB_{1-x}D$ is determined by the ratio of the diffusion flux j_A to the total diffusion flux:

$$x = \frac{j_A}{j_A + j_B}. \tag{63}$$

The A fraction in vapor is given by the ratio of the vapor flux J_A to the total vapor flux:

$$z = \frac{J_A}{J_A + J_B}. \tag{64}$$

Using these definitions in Eq. (62), it is easy to obtain the vapor-solid distribution in the form:

$$z = \frac{x}{c + (1 - c)x}(1 + (1 - x) \times \{cA\exp[\omega(1 - x)^2] - B\exp(\omega x^2)\}), \tag{65}$$

with coefficients:

$$c = \frac{\Lambda_A}{\Lambda_B}, \quad A = \frac{n_A^{\rm eq} n_D^{\rm eq}}{J_{\rm tot} T_A n_D}, \quad B = \frac{n_B^{\rm eq} n_D^{\rm eq}}{J_{\rm tot} T_B n_D}, \tag{66}$$

and $J_{\rm tot} = J_A + J_B$ as the total vapor flux of group-III elements. This general $z(x)$ dependence, along with calculations of its parameters for different systems, is the main result of this paper. The vapor-solid distribution given by Eq. (65) has the same shape as the liquid-solid distribution for VLS III-V ternary nanowires given by Eq. (1) at $f_A(y) = f_B(y) = f_D(y) = 0$, corresponding to a perfect mixture of noninteracting adatoms. This is not surprising because the growth rates of different binaries leading to Eq. (1) were obtained in Ref. [35] using similar considerations for the attachment-detachment rates for a III-V ternary island surrounded by liquid. However, in contrast to the previous works [35,40], our approach leads to the vapor-solid distribution which applies to a wide range of systems rather than the liquid-solid distribution for nanowires (where there are only a few works revealing the compositional correlation between the droplet and nanowire [73]).

Our Eqs. (65) and (66) describe the vapor-solid distribution with well-defined parameters. Indeed, the fluxes $J_{\rm tot}$ and J_D should be precisely controlled in any experimental conditions, at least in the MBE technique. In vapor phase epitaxy techniques such as MOVPE and HVPE, supersaturations of AD and BD gas mixtures with respect to binary solids may be more relevant [27]. The model can easily be adapted to this case, as will be discussed shortly. The quantities $n_A^{\rm eq} n_D^{\rm eq}$ and $n_B^{\rm eq} n_D^{\rm eq}$ defined by Eq. (18) are expressed through the temperature-dependent values $\mu_{AD}^0 - \mu_A^0 - \mu_D^0$ and $\mu_{BD}^0 - \mu_B^0 - \mu_D^0$ which are known for most III-V binaries [74,75]. The binary interaction constants in solid ω are well known [76,77]. The characteristic times T_A and T_B contain the known desorption times of adatoms τ_A and τ_B and geometry of a nanostructure. Finally, the kinetic coefficient c depends on the adatom diffusion lengths λ_A and λ_B and geometrical parameters of a nanostructure or a growth template in SAE, while the corresponding coefficient k for the liquid-solid growth of the binaries was not determined within the kinetic models of Refs. [26,35,37,40]. Although the diffusion lengths λ_i are not exactly known in the general case and influenced by many factors such as temperature and group-V flux or V/III flux ratio, they correspond to a minimum uncertainty in the kinetic constants which is present in the diffusion equations for different populations of group-III adatoms.

According to the analysis of the previous section,

$$c = \frac{\lambda_A}{\lambda_B}\frac{\tanh(P/2\lambda_A)}{\tanh(P/2\lambda_B)}, \tag{67}$$

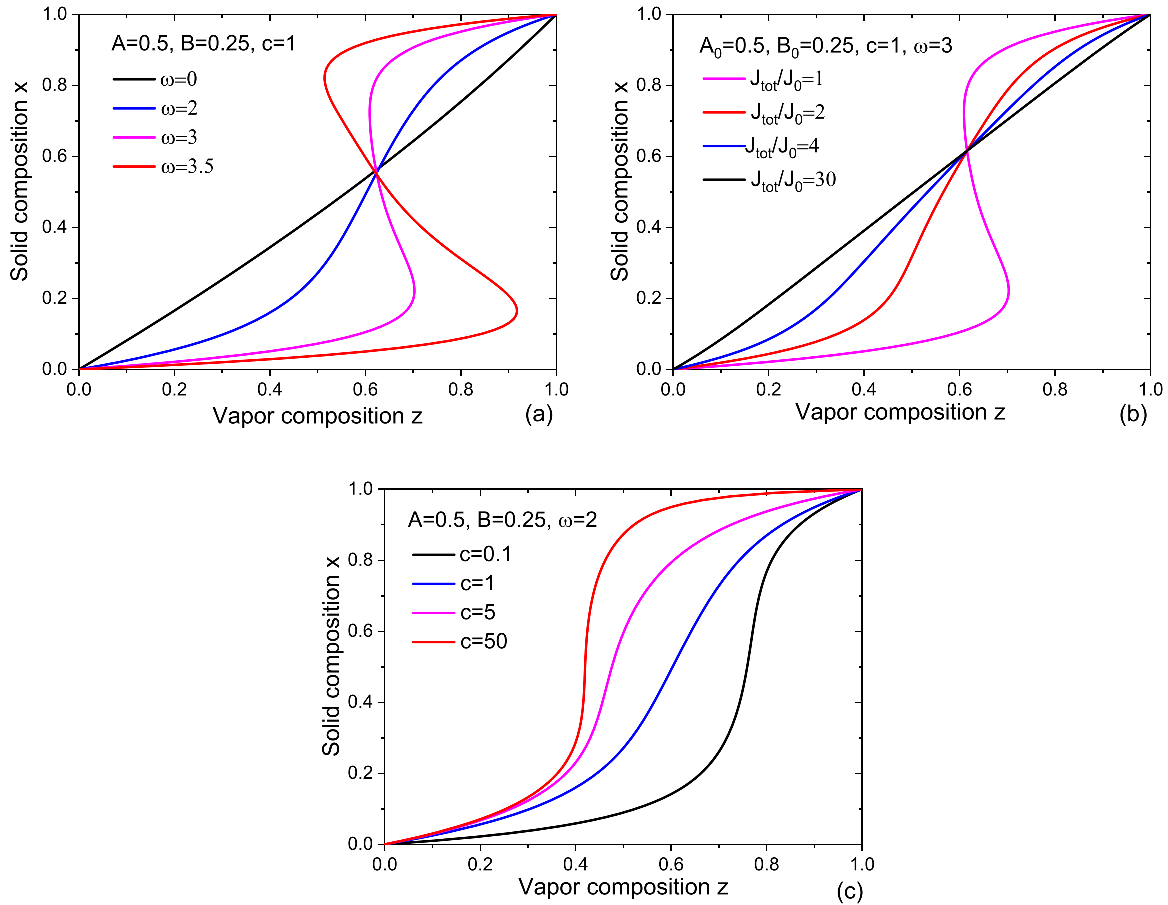

FIG. 3. Vapor-solid distributions obtained from Eqs. (65) and (66) (a) at a fixed $A = 0.5$, $B = 0.25$, $c = 1$, and different ω from 0 to 3.5 shown in the legend; (b) at a fixed $c = 1$ and $\omega = 3$ for different total fluxes of group III adatoms J_{tot}, with the total flux J_0 corresponding to $A_0 = 0.5$ and $B_0 = 0.5$ and the legend showing different ratios J_{tot}/J_0; (c) at a fixed $A = 0.5$, $B = 0.25$, $\omega = 2$, and different c from 0.1 to 50 shown in the legend. The wavy sections of the curves correspond to the miscibility gaps.

for an echelon of steps with separation P, as shown in Figs. 2(a) and 2(b). This c changes from 1 for dense echelons of steps (at $P/2\lambda_i \to 0$) to λ_A/λ_B for a single step (at $P/2\lambda_i \to \infty$). For a planar nanowire growing in a 1D slit of width W shown in Fig. 2(d), we have

$$c = \frac{\lambda_A^2}{\lambda_B^2}\frac{\ln[\cosh(W/\lambda_A)]}{\ln[\cosh(W/\lambda_B)]}. \tag{68}$$

This c changes from 1 for narrow slits with $W/\lambda_i \ll 1$ to λ_A/λ_B for wide slits with $W/\lambda_i \to \infty$. For the vertical nanowire shown in Fig. 2(f),

$$c = \frac{\bar{\Lambda}_A}{\bar{\Lambda}_B} = \frac{\chi_A^+ + \lambda_{fA}/R + (\lambda_{sA}/R)^2}{\chi_B^+ + \lambda_{fB}/R + (\lambda_{sB}/R)^2}. \tag{69}$$

For long enough nanowire or for nanowires grown on unpatterned surfaces, adatom diffusion from the substrate can be neglected [47–49,66]. At $\lambda_{sA} = \lambda_{sB} = 0$ and $\chi_A^+ = \chi_B^+$, c changes from 1 for thick nanowires with $\chi_i^+ \gg \lambda_{fi}/R$ to $\lambda_{fA}/\lambda_{fB}$ for thin nanowires with $\chi_i^+ \ll \lambda_{fi}/R$. The physical meaning of the kinetic coefficient c follows directly from its definition. This coefficient accounts for different attachment rates or direct diffusion fluxes of A and B adatoms into a III-V ternary nanostructure, which is the only reason for the solid composition x being different from the vapor composition z in the absence of detachment processes. Equations (67) to (69) show that the c value varies from 1 to λ_A/λ_B depending on the nanostructure geometry. In these examples, for dense echelons of steps, narrow slits, or thick vertical nanowires, different diffusivities of A and B adatoms are suppressed by geometry and do not influence the solid composition. The situation is reversed for sparce echelons of steps, wide slits, or narrow vertical nanowires, where the kinetically controlled solid composition is determined by the λ_A/λ_B ratio.

Let us now consider the general properties of the vapor-solid distribution given by Eqs. (65) and (66). Figure 3(a) shows how the distribution shape changes with the binary interaction constant ω. These curves approximately correspond to $A_xB_{1-x}D$ materials with different lattice mismatch grown under the same vapor supersaturations with respect to solid binaries AD and BD (described by the fixed $A = 0.5$ and $B = 0.25$) and a fixed total group-III flux I_{tot}. At $\omega = 0$, the vapor-solid distribution is almost linear. Increasing ω leads to pronounced nonlinearity of the curves. The wavy van der Waals loops of the curves at $\omega = 3$ and 3.5 correspond to the miscibility gaps in systems with strong interactions between dissimilar III-V pairs at a growth temperature such as InGaAs and InGaN [7,10,11,26,27,32–34,36–38]. It is noteworthy that

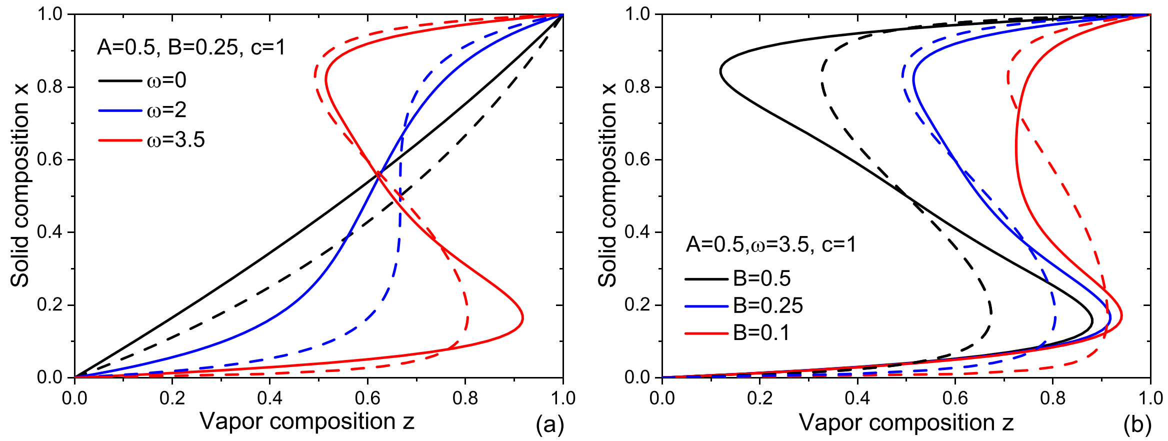

FIG. 4. Vapor-solid distributions obtained from Eqs. (65) and (66) (solid lines) compared with the equilibrium distributions given by Eq. (71) (dotted lines) for (a) a fixed $A = 0.5$, $B = 0.25$, $c = 1$, and different ω from 0 to 3.5 shown in the legend; and (b) a fixed $A = 0.5$, $c = 1$, $\omega = 3.5$, and different B from 0.1 to 0.5 shown in the legend.

the nucleation-limited liquid-solid distributions [32], as well as thermodynamically driven distributions [11,36], develop van der Waals loops at $\omega \geqslant 2$, while our kinetic distribution remains monotonic at $\omega = 2$. Figure 3(b) shows that the miscibility gap in a given ternary material at a given temperature (corresponding to a fixed $\omega = 3$) can be fully circumvented at high enough vapor supersaturations which can be raised, for example, by increasing the total group-III flux J_{tot} or similarly by increasing the group-V flux J_D. In the example shown in Fig. 3(b), the group-V flux J_D is fixed, and the total group-III flux J_{tot} is varied. At a low $J_{\text{tot}} = J_0$ corresponding to $A_0 = 0.5$ and $B_0 = 0.5$ as in Fig. 3(a), the miscibility gap is present. However, increasing the total group-III flux by only a factor of 2 leads to the suppression of the gap. Further increases of J_{tot} make the $x(z)$ curves more linear, matching the simplest $z = x$ dependence at $J_{\text{tot}}/J_0 = 30$. Figure 3(c) shows the dependence of the distribution shape on the kinetic coefficient c at a fixed $\omega = 2$ for $A = 0.5$ and $B = 0.25$. A small c value of 0.1 suppresses the incorporation of AD pairs into a solid, which is why the solid composition x is lower than z. At a large c of 50, the incorporation of AD pairs into a solid is favored, and the x values become larger. The distributions depend strongly on c, showing that the unknown k in Eq. (1) (which is often out to 1 in modeling the data on VLS III-V nanowires [40]) leaves a large uncertainty in the compositional trends.

The equilibrium state in our model corresponds to zero fluxes of both types of adatoms, $j_A = 0$, $j_B = 0$. From Eqs. (62) and (19), these conditions yield

$$J_A = zJ_{\text{tot}} = Ax\exp[\omega(1-x)^2],$$
$$J_B = (1-z)J_{\text{tot}} = B(1-x)\exp(\omega x^2). \tag{70}$$

Dividing J_A by J_B, one obtains the equilibrium vapor-solid distribution in the form:

$$z = \frac{x}{x + (1-x)(B/A)\exp[\omega(2x-1)]}, \quad \frac{B}{A} = \frac{n_B^{\text{eq}} T_A}{n_A^{\text{eq}} T_B}. \tag{71}$$

It is remarkable that the shape of this distribution is exactly equivalent to the nucleation-limited liquid-solid distribution obtained in Ref. [32], where the coefficient B/A depends on the liquid composition y and other parameters of the liquid state. In our approach, the B/A value is proportional to the ratio $n_B^{\text{eq}}/n_A^{\text{eq}} = (\Omega_B/\Omega_A)^{2/3}\exp(\mu_B^0 - \mu_A^0 - \mu_{BD}^0 + \mu_{AD}^0)$, which is a thermodynamic value related to different affinities of A and B atoms [32], and the ratio T_A/T_B which may contain different geometrical parameters of a nanostructure. In this respect, the vapor-solid distribution given by Eq. (71) is not entirely thermodynamic. Rather, it cancels out both diffusion fluxes of adatoms and hence corresponds precisely to the no-growth conditions for a given nanostructure. It will be referred to as the equilibrium distribution in what follows just for brevity.

Figure 4(a) shows a comparison of the vapor-solid distribution given by Eqs. (65) and (66) with the equilibrium distribution for different interaction constants ω. A fixed $c = 1$ corresponds to the absence of purely kinetic effects due to different diffusion lengths of A and B adatoms on the solid composition. As mentioned above, the miscibility gap in the equilibrium distribution opens at $\omega = 2$, while the kinetic distribution is monotonic at this ω. Figure 4(b) shows how the change in the parameter B shifts both distributions at a fixed ω of 3.5. Overall, the kinetic distribution is quite close to the equilibrium one at $c = 1$.

At $A \to 0$ and $B \to 0$, corresponding to a purely kinetic growth regime without negative diffusion fluxes leaving a III-V ternary nanostructure, Eq. (65) is reduced to the Langmuir-McLean formula [79]:

$$z = \frac{x}{c + (1-c)x}, \quad x = \frac{cz}{1 + (c-1)z}, \tag{72}$$

which shape is determined solely by the coefficient c. In Refs. [24,32], it was argued that this simple distribution applies to lattice-matched systems with weak interactions between dissimilar III-V pairs such as AlGaAs. The equilibrium vapor-solid distribution given by Eq. (71) is indeed reduced to Eq. (72) at $\omega = 0$. The kinetic distribution given by Eq. (65) at $\omega = 0$ takes a more complex form:

$$z = \frac{x}{c + (1-c)x}[1 + (cA - B)(1-x)]. \tag{73}$$

Here, the flux-dependent constants A and B enter separately rather than through their ratio in Eq. (71). Figure 5 shows

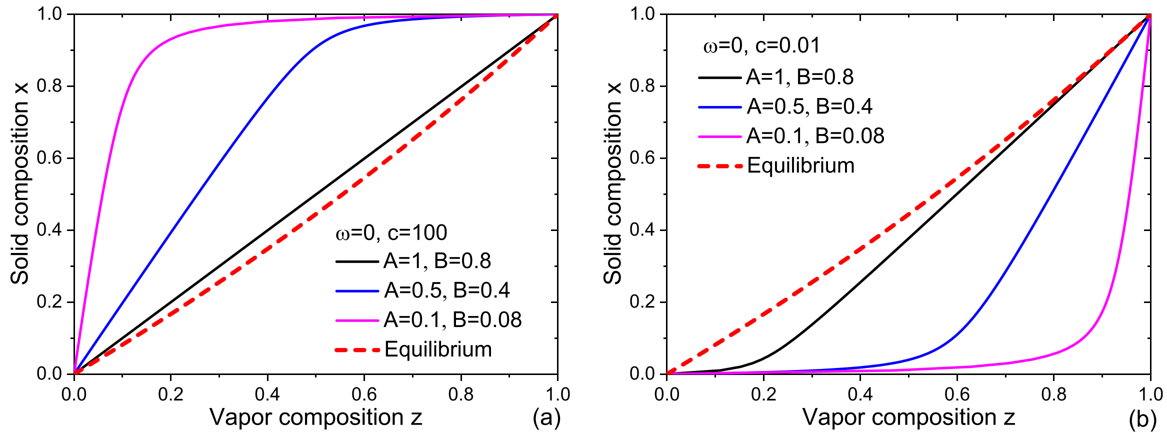

FIG. 5. Vapor-solid distributions at $\omega = 0$ (solid lines) compared with the equilibrium distribution at $\omega = 0$ and a fixed B/A of 0.8 (dashed lines) at (a) $c = 100$ and (b) $c = 0.01$ for different A and B shown in the legends.

that the kinetic vapor-solid distribution can be very different from the equilibrium distribution (which remains the same at a fixed B/A of 0.8) even at $\omega = 0$. The difference depends on the parameter c. At a large c of 100, corresponding to the predominant diffusion transport of A adatoms into a nanostructure [Fig. 5(a)], the kinetic distribution is close to equilibrium only at large $A = 1$ and $B = 0.8$. Decreasing A and B by a factor of 10 leads to a strongly nonlinear $x(z)$ dependence, with $x \gg z$ in the entire range of compositions. At a small c of 0.01, corresponding to the predominant diffusion transport of B adatoms [Fig. 5(b)], the situation is reversed. Large A and B values yield a close-to-equilibrium composition in the solid state, while decreasing A and B by a factor of 10 leads to a pronounced asymmetry in the distribution where the x value is strongly suppressed.

As mentioned above, the total flux of group-III adatoms $J_{\rm tot}$ is not necessarily fixed in the growth experiments with variable vapor composition z. According to Eq. (66), the coefficients A and B can be presented in the form:

$$A = \frac{z}{S_{AD}}, \quad S_{AD} = J_A \frac{T_A}{n_A^{\rm eq}} \frac{n_D}{n_D^{\rm eq}} = \frac{J_A}{J_A^{\rm eq}} \sqrt{\frac{J_D}{J_D^{\rm eq}}},$$

$$B = \frac{1-z}{S_{BD}}, \quad S_{BD} = J_B \frac{T_B}{n_B^{\rm eq}} \frac{n_D}{n_D^{\rm eq}} = \frac{J_B}{J_B^{\rm eq}} \sqrt{\frac{J_D}{J_D^{\rm eq}}}, \tag{74}$$

where the vapor fluxes J_A and J_B can now be varied arbitrary without maintaining a constant $J_{\rm tot} = J_A + J_B$. The quantities S_{AD} and S_{BD} in these expressions stand for the effective supersaturations of AD and BD gas mixtures with respect to solid nanostructures. The equilibrium vapor fluxes $J_i^{\rm eq} = n_i^{\rm eq}/T_i$ for $i = A, B$ contain the characteristic times T_i which account for nanostructure geometry. Therefore, the S_{AD} and S_{BD} values are generally different from vapor supersaturations with respect to planar AD and BD layers. Equation (74) is written for group-V desorption in the form of dimers. In MOVPE and HVPE techniques, the group-V precursors such as AsH_3 or NH_3 contain only one group-V atom. A more relevant form of vapor supersaturations in this case could be

$$S_{AD} = \frac{J_A J_D}{J_A^{\rm eq} J_D^{\rm eq}}, \quad S_{BD} = \frac{J_B J_D}{J_B^{\rm eq} J_D^{\rm eq}}, \tag{75}$$

with $J_D = n_D/\tau_D$ and $J_D^{\rm eq} = n_D^{\rm eq}/\tau_D$. Note that the S_{AD} and S_{BD} values are influenced by the patrial pressures of carrier gas H_2 and HCl in the case of HVPE [26,27].

Using Eq. (74) in Eq. (65), we obtain a more general form of the vapor-solid distribution:

$$z = \frac{x[1-(1-x)\exp(\omega x^2)/S_{BD}]}{c+(1-c)x - x(1-x)\{c\exp[\omega(1-x)^2]/S_{AD} + \exp(\omega x^2)/S_{BD}\}}, \tag{76}$$

with the two supersaturations for AD and BD binary vapor-solid systems. This representation holds regardless of the forms of S_{AD} and S_{BD} in MBE, MOVPE, or HVPE techniques. Of course, this distribution is reduced to Eq. (65) when $J_{\rm tot}$ is independent of z. Otherwise, the A and B parameters in Eq. (65) depend on the vapor composition z as given by Eq. (74), which is equivalent to Eq. (76). According to Eq. (76), the solid composition can be tuned by varying independently the binary supersaturations S_{AD} and S_{BD}, as shown in Fig. 6. A ternary system with $\omega = 2.5$ has a thermodynamically forbidden miscibility gap. When both supersaturations are large and equal each other ($S_{AD} = S_{BD} = 100$), the gap is suppressed by fast growth kinetics, as we saw earlier in Fig. 3(b). The vapor-solid distribution is linear and follows the simplest kinetic law $x = z$ at $c = 1$. When the supersaturation for AD binary system S_{AD} is decreased at a constant $S_{BD} = 100$, incorporation of AD pairs into a growing $A_xB_{1-x}D$ structure becomes unfavorable. This leads to lower x values in the entire range of compositions. Finally, at a low S_{AD} of 1.03, the miscibility gap is developed for large

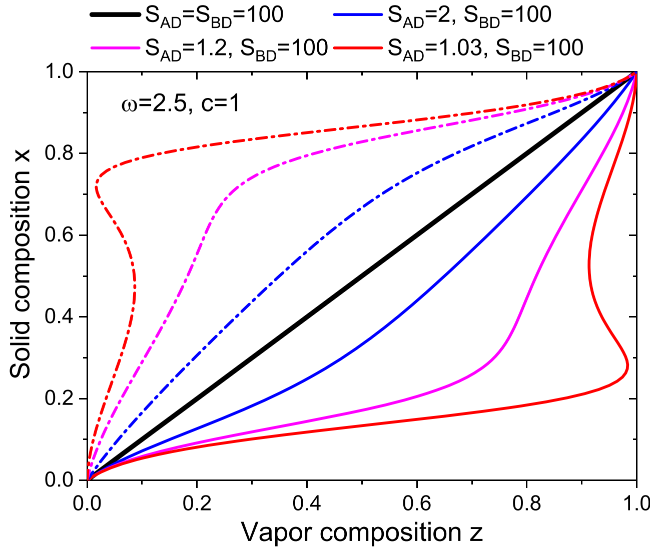

FIG. 6. Vapor-solid distributions obtained from Eq. (76) at a fixed $\omega = 2.5$, $c = 1$ and different supersaturations S_{AD} and S_{BD} shown in the legend (solid lines). Dash-dotted lines correspond to the inversion of S_{AD} and S_{BD} values.

x, meaning that high AD contents are hardly accessible in this growth regime. Inversion of the binary supersaturations, that is, keeping a high value of $S_{AD} = 100$ and decreasing the S_{BD} value leads to the opposite behavior. The curves at the fixed S_{BD} and S_{AD} in Fig. 6 are symmetrical with respect to $x = z$.

The equilibrium and nucleation-limited compositional maps with the miscibility gaps should be corrected to exclude the wavy regions of the curves by applying the Maxwell rule. The straight line on the distributions is constructed in such a way that the areas of the van der Waals loops above and below the line are equal each other. This position of the line corresponds to equal chemical potential differences for AD and BD binaries [32]. We suspect that the same rule applies in the kinetically controlled regime studied here. However, the justification of the Maxwell rule for the kinetic vapor-solid distributions is not obvious and requires a separate treatment which will be presented elsewhere.

The obtained vapor-solid distribution should work equally well for nonstoichiometric binary materials A_xB_{1-x} such as Si_xGe_{1-x} [80,81]. In the above treatment, ternary $A_xB_{1-x}D$ materials were based on the intermix of surface diffusive group-III elements A and B, while the influence of a group-V element D under group-V-rich growth conditions remained only in thermodynamic constant n_D^{eq} and group-V adatom concentration n_D. Therefore, the model is reduced to a binary A_xB_{1-x} system by putting $n_D = n_D^{eq}$. The vapor-solid distribution for A_xB_{1-x} binaries is then given by Eqs. (65) and (66) with

$$A = \frac{n_A^{eq}}{J_{tot}T_A}, \quad B = \frac{n_B^{eq}}{J_{tot}T_B}. \tag{77}$$

Equation (18) for n_A^{eq} and n_B^{eq} takes the simple form:

$$n_A^{eq} = \frac{1}{\Omega_A^{2/3}}\exp\left(\frac{\mu_A^s - \mu_A^l}{k_BT}\right), \quad n_B^{eq} = \frac{1}{\Omega_B^{2/3}}\exp\left(\frac{\mu_B^s - \mu_B^l}{k_BT}\right), \tag{78}$$

TABLE I. Affinities of Ga with respect to In in InGaAs and InGaP systems.

T (°C)	$\exp[(\Delta\mu^0_{GaAs} - \Delta\mu^0_{InAs})/k_BT]$	$\exp[(\Delta\mu^0_{GaP} - \Delta\mu^0_{InP})/k_BT]$
440	0.011	0.00138
460	0.0128	0.00165
480	0.0148	0.00196
570	0.0262	0.00379
750	0.0612	0.00944

where μ_i^s and μ_i^l are the chemical potentials of pure solid and liquid elements $i = A, B$.

VI. InGaAs AND InGaP SYSTEMS

Thermodynamic data for InGaAs and InGaP ternary systems can be found in Refs. [74–77]. The most important parameters used in calculations are given in the Supplemental Material [78]. The limiting case of $B/A \to 0$ in Eq. (65) or $S_{BD}/S_{AD} \to 0$ in Eq. (76) is usually a good approximation for the kinetically controlled composition of InGaAs and InGaP ternaries and will be used in what follows. The strong inequality $A \gg B$ for these material systems follows from different affinities of In and Ga, given by the exponentials of the chemical potential differences $\Delta\mu_{AD}^0 = \mu_{AD}^0 - \mu_A^0 - \mu_D^0$ and $\Delta\mu_{BD}^0 = \mu_{BD}^0 - \mu_B^0 - \mu_D^0$ in Eq. (18) for A = In, B = Ga, and D = As or P. This feature is well known and was discussed for the InGaAs system in Ref. [32]. According to Eqs. (66) and (18), the ratio B/A is given by

$$\frac{B}{A} = \left(\frac{\Omega_A}{\Omega_B}\right)^{2/3}\frac{T_A}{T_B}\exp\left(\frac{\Delta\mu_{BD}^0 - \Delta\mu_{AD}^0}{k_BT}\right). \tag{79}$$

In atoms are known to desorb more easily than Ga, which is why the ratio T_{In}/T_{Ga} should be less than unity in most cases. Table I gives the values of the exponential term in Eq. (79) for InGaAs and InGaP systems calculated using the data of the Supplemental Material [78] for different temperatures. It is seen that the $\exp[(\Delta\mu_{BD}^0 - \Delta\mu_{AD}^0)/k_BT]$ terms and hence the B/A values are extremely small in both cases. Therefore, the B term in Eq. (65) can be safely neglected in a wide range of temperatures for these ternary systems.

The simplified form of Eq. (65) at $B = 0$ is given by

$$z = \frac{x}{c + (1-c)x}\{1 + (1-x)cA\exp[\omega(1-x)^2]\}. \tag{80}$$

This vapor-solid distribution generally applies to systems with different affinities of A and B atoms. It is interesting to note that the B/A ratio, even very small compared with unity, can never be neglected in the equilibrium or nucleation-limited distribution given by Eq. (71). Rather, the composition of the mother phase should be made very close to unity to obtain any nonnegligible x content in a solid. This feature was demonstrated for VLS InGaAs nanowires in Refs. [32,33] for the liquid-solid distributions $x(y)$, where the In contents in liquid droplets were >0.97. Figure 7 shows the vapor-solid distributions for the InGaAs system at 440 °C, where ω = 2.4. The equilibrium distribution presents the miscibility gap. According to this diagram, obtaining any reasonable InAs

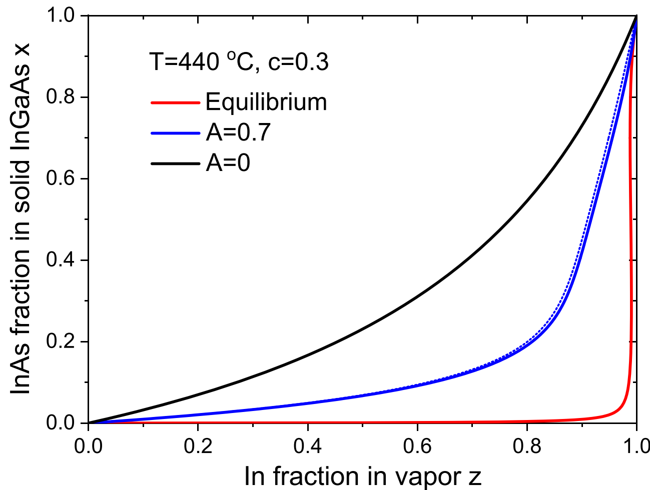

FIG. 7. Vapor-solid distributions for InGaAs system at 440 °C, fixed $c = 0.3$, and different A, compared with the equilibrium distribution. The dotted line is obtained from Eq. (80) at $B = 0$ and is indistinguishable from the curve given by Eq. (65).

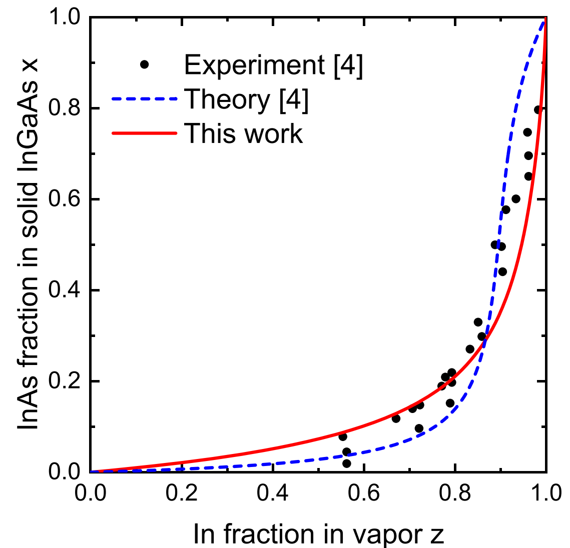

FIG. 8. Vapor-solid composition for planar InGaAs layers of Ref. [4] (symbols), fitted by Eq. (65) with the parameters given in Table II (solid line). Dashed line shows the fit by the model of Ref. [4].

fractions in solid InGaAs in the near-equilibrium regime is very difficult and requires very large z corresponding to an almost negligible fraction of Ga in vapor. Growth at $A = 0.7$ corresponds to low group-III fluxes and InGaAs growth rates. However, there is no miscibility gap in this regime, and the $x(z)$ curve becomes smooth. Growth at $A = 0$ corresponds to the purely kinetic regime, in which lower In fractions in a solid are due to a shorter diffusion length of In adatoms at $c = 0.3$. Any InAs fraction in solid InGaAs is easily accessible in the kinetically controlled growth regimes.

VII. THEORY AND EXPERIMENT

In this section, the obtained vapor-solid distribution is used for modeling the stationary compositions of III-V ternary systems based on the group-III intermix. The model parameters used for the fits are given in Table I for each system. Depending on whether or not the total group-III flux J_{tot} was kept constant in the growth experiments, we used the vapor-solid distributions given by Eq. (65) or Eq. (76), respectively. For a fixed J_{tot}, the fitting parameters are A and B in Eq. (65). For variable J_{tot}, the fitting parameters are S_{AD} and S_{BD} in Eq. (76).

$In_xGa_{1-x}As$ layers of Ref. [4] were grown by vapor phase epitaxy in an (In-Ga)-$AsCl_3$-As-H_2 system with the In-Ga metal source producing the chloride precursors InCl and GaCl, and As_4 vapor in the carrier gas H_2. The growth temperature was fixed at 750 °C. Different solid composition x of the layers were achieved by varying the molar ratio of In in the metal In-Ga source and relating it to the In content in vapor z at the known partial pressure of As_4. Figure 8 shows the experimental vapor-solid distribution for InGaAs layers obtained in Ref. [4]. The variation of the solid composition of $In_xGa_{1-x}As$ layers with the vapor composition was described within a model, which assumed close-to-equilibrium growth conditions with 100% decomposition of gaseous precursors leading to the formation of InAs and GaAs pairs [4]. The activities of InAs and GaAs binaries were obtained using the regular solution model. The resulting vapor-solid distribution of Ref. [4] had the form of Eq. (71), in which the ratio B/A is replaced by the ratio of equilibrium constants $K_{\text{InAs}}/K_{\text{GaAs}}$. The curve obtained in Ref. [4] is shown by the dashed line in Fig. 8. This curve is exactly identical to our equilibrium vapor-solid distribution given by Eq. (71) at $T_B/T_A = 0.5$. The solid curve in Fig. 8 shows the fit by Eq. (65) at $B = 0$ as discussed above [which is reduced to Eq. (80)], with $A = 0.7$, and $c = 0.12$. The value of the InAs-GaAs binary interaction constant in thermal units at 750 °C ($\omega = 1.41$) is calculated based on the data in the Supplemental Material [78]. The best fit to the data shown in Fig. 8 requires a large A of 0.7 and a small kinetic constant c of 0.12. The large value of A is explained by the enhanced desorption of In, yielding a short desorption time τ_{In}. The small value of c is due to a shorter diffusion length of In adatoms with respect to Ga ones at the high growth temperature. Overall, the compositional trend in Fig. 8 is like the kinetic diagrams in Fig. 7. InAs fractions in a solid are systematically lower than In fractions in vapor, but the entire compositional range of solid $In_xGa_{1-x}As$ is accessible. Overall, the kinetic model fits the data better than the equilibrium curve given by Eq. (71).

Catalyst-free vertical InGaAs nanowires of Ref. [21] were obtained through the van der Waals epitaxy mechanism by MOVPE on graphene surfaces at 570 °C and a high V/III flux ratio of 20, which guarantees the group-III limited growth regime. These nanowires had a mean length of 3.4 μm, mean radius of 43.5 nm, and surface density of 7×10^8 cm^{-2}. Figure 9 shows the measured vapor-solid distribution and the fit by Eq. (65) at $A = 0.52$, $B = 0$, and $c = 4$. The fit is good for all the datapoints except the datapoint for the lowest z and x, which seems to overestimate the InAs content in nanowires due to parasitic structures on the surface which contribute into the compositional analysis [21]. The A value of 0.52 is lower than in the previous case due to a lower substrate temperature and longer desorption time of In atoms. A large value of c is

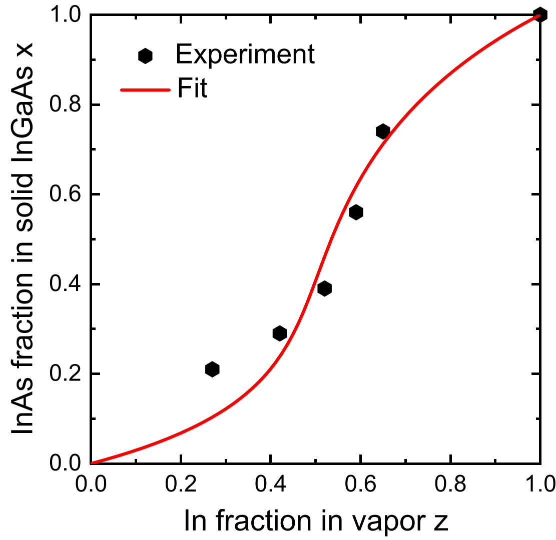

FIG. 9. Vapor-solid composition of selective area epitaxy (SAE) InGaAs nanowires of Ref. [21] (symbols), fitted by Eq. (65) with the parameters given in Table II.

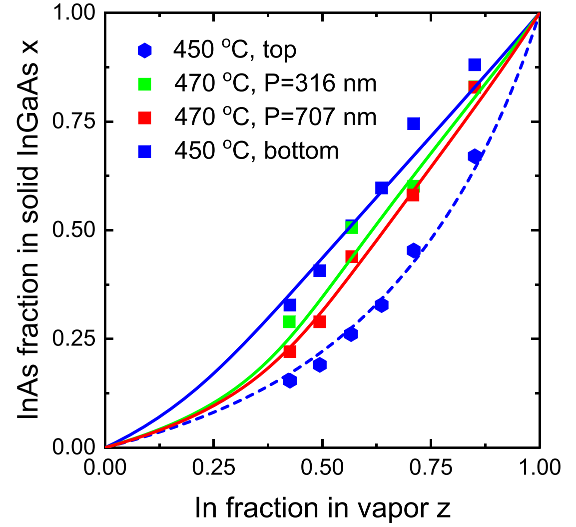

FIG. 10. Vapor-solid composition of Au-catalyzed vapor-liquid-solid (VLS) InGaAs nanowires of Ref. [16] (symbols), fitted by Eq. (65) with the parameters given in Table II. Pitch P in the legend corresponds to the average distance between the nanowires.

required to fit the data. These nanowires are long enough to neglect the group-III adatom diffusion from the substrate, in which case Eq. (69) at $\chi_{\rm In}^{+} = \chi_{\rm Ga}^{+} = 1$ for the flat tops of SAE nanowires is reduced to

$$c = \frac{R + 2\lambda_{\rm In}}{R + 2\lambda_{\rm Ga}}. \quad (81)$$

Here, we write the effective diffusion lengths in the form $\lambda_{if} = 2\lambda_i$ for i = In and Ga, with λ_i as the diffusion lengths on the nanowire sidewalls. At $c = 4$ and $R = 43.5$ nm, this yields a linear relationship between the In and Ga adatom diffusion lengths: $\lambda_{\rm In} = 65\ {\rm nm} + 4\lambda_{\rm Ga}$. Therefore, the In diffusion lengths on the nanowire sidewalls is larger than the Ga one and is >65 nm in the experimental MOVPE conditions at 570 °C.

Au-catalyzed InGaAs nanowires of Ref. [16] were grown by MOVPE using 50-nm-diameter Au aerosol nanoparticles deposited onto InAs(111)B substrates. Different vapor compositions were achieved by changing the fluxes of TMIn and TMGa precursors. For 3-µm-long nanowires grown at 450 °C with a V/III flux ratio of 12.6, the composition was measured at the top and bottom. The average distance between these nanowires was 707 nm. At a temperature of 470 °C and a V/III flux ratio of 6.32, 1.2-µm-long InGaAs nanowires were grown with two different surface densities of Au nanoparticles corresponding to the average distance between the nanowires of 316 nm (dense nanowires in Table II) and 707 nm (sparse nanowires in Table II). For these nanowires, the composition was measured at the top. Figure 10 shows the measured compositions and their fits by the model.

It is seen that the difference in the measured compositions is larger for the tops and bottoms of the same nanowires grown at 450 °C than between the nanowires grown at different temperatures. The vapor-solid composition at the nanowire top at 450 °C is almost linear and close to $x = z$, while it is strongly nonlinear at the nanowire bottom, with $x < z$. The fitting values of A decrease for lower temperatures according to Table II, as it should be due to lower desorption rates at lower T. Within the model, the large difference between the composition in the top and bottom of the nanowires is explained by different transport mechanisms of group-III adatoms. According to Refs. [41,66,68,82], long nanowires are fed by adatoms diffusing from the nanowire sidewalls and directly impinging

TABLE II. Parameters of III-V ternary systems.

Ref.	System	T (°C)	ω	A	B	S_{AD}	S_{BD}	c
[4]	Planar $In_xGa_{1-x}As$ layers	750	1.4119	0.7	0			0.12
[21]	Catalyst-free $In_xGa_{1-x}As$ nanowires on graphene	570	1.9064	0.52	0			4
[16]	Dense Au-catalyzed VLS $In_xGa_{1-x}As$ nanowires on InAs(111)B	470	2.2846	0.25	0			0.98
[16]	Sparse Au-catalyzed VLS $In_xGa_{1-x}As$ nanowires on InAs(111)B	470	2.2846	0.25	0			0.85
[16]	Tops of Au-catalyzed VLS $In_xGa_{1-x}As$ nanowires on InAs(111)B	450	2.3728	0.1	0			0.95
[16]	Bottoms of Au-catalyzed VLS $In_xGa_{1-x}As$ nanowires on InAs(111)B	450	2.3728	0.1	0			0.35
[25]	0.3-µm-long Au-catalyzed VLS $In_xGa_{1-x}P$ nanowires on InP(111)B	440	2.5949		0	3.57	∞	7
[25]	1-µm-long Au-catalyzed VLS $In_xGa_{1-x}P$ nanowires on InP(111)B	460	2.5145		0	1.11	∞	1.5
[25]	3-µm-long Au-catalyzed VLS $In_xGa_{1-x}P$ nanowires on InP(111)B	480	2.4385		0	0.57	∞	0.9
[20]	Cores of Au-catalyzed VLS $Al_xGa_{1-x}As$ nanowires on GaAs(111)B	510	0	0	0			0.385

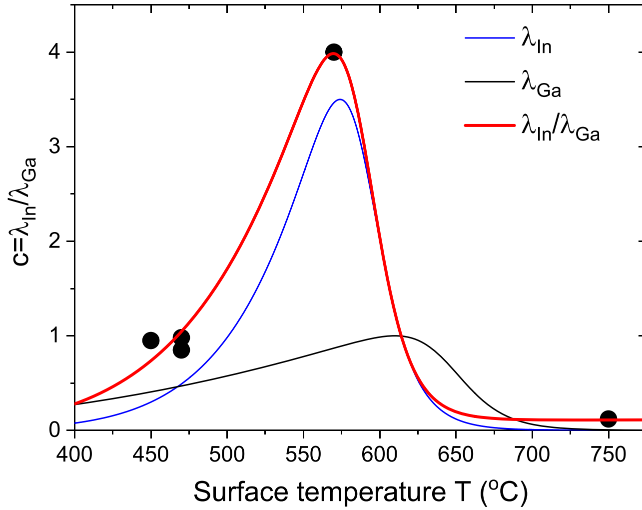

FIG. 11. In and Ga adatom diffusion lengths and their ratio, fitted by Eq. (83). The diffusion lengths are normalized to a maximum of λ_{Ga} at 610 °C.

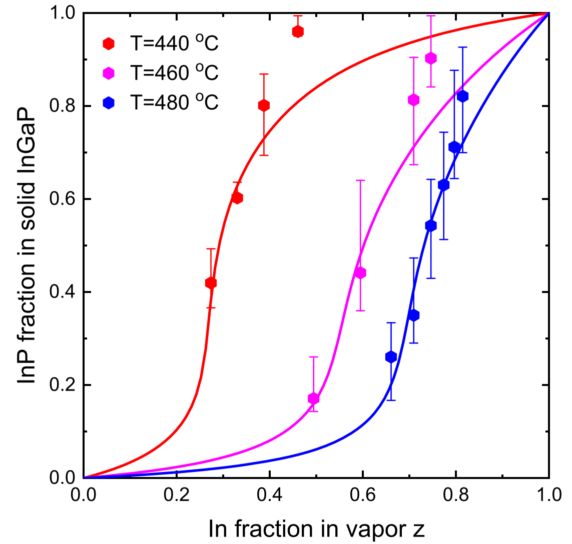

FIG. 12. Vapor-solid composition of Au-catalyzed vapor-liquid-solid (VLS) InGaP nanowires of Ref. [25] (symbols), fitted by Eq. (76) with the parameters given in Table II.

onto the droplet surface. Conversely, short nanowires, which become nanowire bottoms later, are fed mainly by surface diffusion from the substrate surface. Equation (69) for VLS growth by MOVPE is then reduced to

$$c = \frac{R + (1 + \cos\beta)\lambda_{\rm In}}{R + (1 + \cos\beta)\lambda_{\rm Ga}}, \quad c = \left(\frac{\lambda_{s,\rm In}}{\lambda_{s,\rm Ga}}\right)^2, \tag{82}$$

for nanowire bottoms and tops, respectively. According to Table II, the fitting values of c are close to unity for all nanowire tops, meaning that surface diffusion of In and Ga adatoms from the nanowire sidewalls is similar (or even negligible compared with the direct vapor fluxes). The c value equals 0.35 for the nanowire bottoms, corresponding to $\lambda_{s,\rm In} = 0.59\lambda_{s,\rm Ga}$ on the substrate surface at 450 °C.

Figure 11 shows a plot of the c values vs temperature for the InGaAs system according to Table II. It is seen that the $c(T)$ dependence exhibits a maximum of ~ 4 at a temperature of 570 °C. For lower temperatures in the range from 450 to 470 °C, the c values are on the order of unity, whereas the c value at 750 °C is only 0.12. Although the surfaces on which group-III adatoms diffuse are different, the c value is related to the ratio of the effective diffusion lengths of In adatoms over Ga ones: $c = \lambda_{\rm In}/\lambda_{\rm Ga}$. For vertical III-V nanowires, the diffusion length on the nanowire sidewalls can be limited by either desorption or incorporation into the surface steps [41,50]. Desorption rate increases for higher temperatures, while surface incorporation and the radial growth rate increase for lower temperatures. As a result, the effective diffusion length of group-III adatoms has a maximum at a certain temperature ($\sim$ 600 °C for Ga adatoms on the sidewalls of binary GaAs and GaP nanowires) [83]. It is well known that In diffuses faster than Ga at low enough temperatures but also desorbs at lower temperatures than Ga [41]. The curves in Fig. 11 show the normalized diffusion lengths of In and Ga adatoms obtained from the expression given in Ref. [83]:

$$\lambda_i(T) = \lambda_i(T_i)\frac{B_i + C_i}{B_i \exp\left[-\left(C_i\frac{T_i}{T} - 1\right)\right] + C_i \exp\left[B_i\left(\frac{T_i}{T} - 1\right)\right]}, \tag{83}$$

for i = In and Ga. Here, $T_{\rm In} = 560$ °C and $T_{\rm Ga} = 610$ °C are the temperatures corresponding to the maximum diffusion lengths of In and Ga adatoms, respectively, and B_i and C_i are the dimensionless coefficients related to the activation energies for desorption and surface diffusion [83]. It is seen that this model reproduces quite well the general trend for the temperature behavior of $c = \lambda_{\rm In}/\lambda_{\rm Ga}$.

Au-catalyzed InGaP nanowires of Ref. [25] were grown by MOVPE on InP(111)B substrates using the randomly dispersed 80-nm-diameter Au nanoparticles. The growth was performed at different temperatures from 440 to 480 °C under group-V-rich conditions. These nanowires had a surface density of 4×10^8 cm^{-2}, corresponding to an average distance between the nanowires of 500 nm and different lengths of 0.3, 1, and 3 μm at T = 440, 460, and 480 °C, respectively. Different vapor compositions were achieved by varying TMIn flux at a constant TMGa flux, so that the total group III flux was increased. Consequently, we used Eq. (76) for fitting the data. Figure 12 shows the measured compositions and their fits by the model. According to Table II, the value of $A_0 = 0.28$ (corresponding to a fixed total group-III flux) at $S_{AD} = 3.57$ at 440 °C is almost three times larger than the corresponding A = 0.1 for InGaAs nanowires at a similar temperature of 450 °C. This is explained by the fact that, at similar nanowire radii and under similar material fluxes of group-III and V species, the ratio $A_{\rm InGaP}/A_{\rm InGaAs}$ approximately equals $n_{\rm In}^{\rm eq} n_{\rm P}^{\rm eq}/n_{\rm In}^{\rm eq} n_{\rm As}^{\rm eq}$. This ratio is ~3 in the temperature range from 440 to 480 °C according to thermodynamic data given in the Supplemental Material [78]. The fitting values of supersaturation $S_{AD} = S_{\rm InP}$ decrease with temperature. At the highest temperature of 480 °C, $S_{\rm InP} = 0.57$ is below unity, which would correspond

to the absence of growth for pure InP. However, the actual flux of InP into InGaP nanowires remains positive due to a lower chemical potential of the ternary material in this compositional range compared with binary InP.

A large fitting value of $c = 7$ is required to reproduce the compositional data at 440 °C, while at 460 and 480 °C, the c values are on the order of unity, as at the tops of the InGaAs nanowires at similar temperatures of 450 and 470 °C. Short InGaP nanowires at 440 °C (with a length of only 0.3 μm) should grow by surface diffusion of group-III adatoms from the substrate, while longer nanowires at higher T should grow by the direct impingement and surface diffusion from the nanowire sidewalls [66,68,82]. According to Eq. (82), the diffusion lengths of In and Ga adatoms on the sidewalls of InGaP nanowires are similar, as in the case of InGaAs nanowires. On the other hand, our model results in a longer diffusion length of In adatoms on InP(111)B (corresponding to $\lambda_{s,\mathrm{In}} = 2.65\lambda_{s,\mathrm{Ga}}$), while on an InAs(111)B substrate this relationship is reversed ($\lambda_{s,\mathrm{In}} = 0.59\lambda_{s,\mathrm{Ga}}$). The reason for this sharp change is not clear but may be related to different surface treatment procedures used [16,25] or different pyrolysis efficiencies of TMIn and TMGa at 440 °C. Finally, one data point at 440 °C is too close to pure InP at a low z of 0.47 and cannot be fitted by the model. This data point may not be representative due to parasitic structures and planar nanowires emerging on the substrate with uncontrolled composition when the In input is increased at the lowest growth temperature studied in Ref. [25]. Overall, the vapor-solid distributions in InGaP nanowires in Fig. 12 are more nonlinear than InGaAs nanowires in Fig. 11 and favor In incorporation from vapor to solid.

Au-catalyzed VLS AlGaAs nanowires of Ref. [20] were grown by MBE on Si(111) substrates at 510 °C. The Au droplets were obtained by thermal dewetting of thin Au films deposited onto the substrates in a separate vacuum chamber. Parasitic growth of AlGaAs was observed on the unpatterned Si surface between the nanowires. Different vapor compositions z were obtained by varying the Al and Ga fluxes at a fixed total group-III flux corresponding to the equivalent AlGaAs growth rate of 0.3 nm/s, with a V/III flux ratio of 3. Spontaneous formation of the core-shell AlGaAs structures was observed, with higher AlAs fractions in the shells. Cylindrical cores were formed by the VLS mechanism, while conical shells were grown after in the vapor-solid mode. Figure 13 shows the measured AlAs fractions in the cores and shells of AlGaAs nanowires vs the Al fraction in vapor. At a low growth temperature of 510 °C, Al and Ga adatoms are very stable on any surface in MBE growth. Therefore, the composition of the core can be described by the Langmuir-McLean formula given by Eq. (72), corresponding to $A \to 0$ and $B \to 0$. The only fitting parameter c equals 0.385 [20]. This yields the excellent fit to the measured compositions of the nanowire cores, as shown in Fig. 13. With a core radius of 20 nm and a droplet contact angle of 120 °, the linear relationship between the two diffusion lengths on the nanowire sidewalls has the form $\lambda_{\mathrm{Ga}} = 135\ \mathrm{nm} + 2.6\lambda_{\mathrm{Ga}}$ regardless of z [20], showing that the diffusion length of Ga is systematically larger than Al at 510 °C.

Let us now discuss the composition of AlGaAs shells. As mentioned above, the surface diffusivity of group-III adatoms

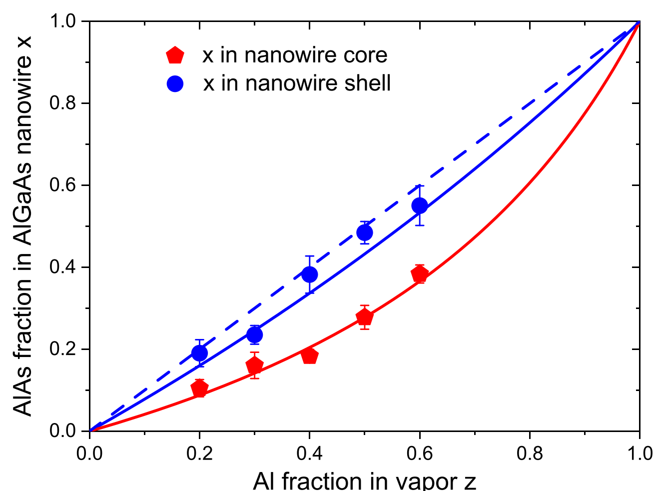

FIG. 13. Vapor-solid composition in the core-shell Au-catalyzed vapor-liquid-solid (VLS) AlGaAs nanowires of Ref. [20] (symbols), fitted by Eq. (76) with the parameters given in Table II. Dashed line corresponds to $x = z$.

in this case should be limited by the step flow on the nanowire sidewalls, as shown in Fig. 1(b). According to Ref. [20], the tapering angle of AlGaAs shells increased and the nanowire length decreased with z. In all cases, the tapering angles were $>3^\circ$, corresponding to pitches $P < 20$ nm from geometrical considerations. If we assume that the diffusion length of Al is much larger than P in all cases, Eq. (67) gives $c = 1$ and $x = z$, meaning that the Al content in the nanowire shells is the same as in vapor. Another way of modeling is to assume that the separation between the steps determines the diffusion length of Al adatoms λ_{Al}. In this model, the steps are formed by crystallization of AlAs pairs and are transparent for Ga adatoms whose diffusion length is larger. At $P = 2\lambda_{\mathrm{Al}}$, Eq. (67) gives

$$c = \frac{\lambda_{\mathrm{Al}}}{\lambda_{\mathrm{Ga}}} \frac{\tanh(1)}{\tanh(\lambda_{\mathrm{Al}}/\lambda_{\mathrm{Ga}})}. \quad (84)$$

The ratio $\lambda_{\mathrm{Al}}/\lambda_{\mathrm{Ga}}$ varies with the vapor composition z, as follows from the measured axial nanowire growth rates. According to the analysis of Ref. [20], $\lambda_{\mathrm{Al}} = 250$ nm and $\lambda_{\mathrm{Ga}} = 780$ nm at $z = 0.2$, decreasing to $\lambda_{\mathrm{Al}} = 8$ nm and $\lambda_{\mathrm{Ga}} = 156$ nm at $z = 0.6$. Therefore, $\lambda_{\mathrm{Al}}/\lambda_{\mathrm{Ga}} \ll 1$ is a good approximation in all cases, which reduces Eq. (84) to $c = 0.762$. The corresponding vapor-solid distribution is shown in Fig. 13 and only slightly underestimates the AlAs fraction in the nanowire shells, while the simple approximation $z = x$ slightly overestimates the measured composition.

VIII. CONCLUSIONS

In conclusion, it has been shown that the stationary composition of a wide range of III-V ternary materials based on the intermix of diffusive group-III elements, from planar layers to nanowires, can be described by the general kinetically controlled vapor-solid distribution. The coefficients of this distribution depend on the nanostructure geometry and contain kinetic constants such as diffusion lengths of group-III adatoms on different surfaces. Thermodynamics of the

material system manifests in the chemical potentials of pure liquids and binaries and in the binary interaction constant in a solid. The equilibrium solutions for the diffusion fluxes reduce the obtained distribution to the thermodynamically controlled or nucleation-limited composition. The experimental vapor-solid distributions in very different ternary III-V systems have been reproduced using the kinetic approach, while none of the systems appear close to thermodynamic behavior. The miscibility gaps of all InGaAs ternaries below the critical temperature are circumvented by the growth kinetics. The developed theory is not restricted to III-V ternaries and should work equally well for SiGe binaries and other material systems. Further consideration should be given to strain-induced effects in lattice-mismatched ternary systems and during growth of III-V nanomaterials on dissimilar Si substrates. While the lattice mismatch is present in a binary interaction constant, we did not consider explicitly its influence on the intermixing, crystal morphologies, growth anisotropy, surface energies, and kinetic constants entering the diffusion equations. We plan to apply these results to catalyst-free InGaN nanostructures and nanowires and to develop a time-dependent model for modeling the interfacial abruptness and compositional profiles across different heterostructures. We also plan to consider the growth process under an arbitrary V/III flux ratio rather than under group-V-rich conditions for ternaries based on group-III intermix. This important extension of the developed approach should enable modeling of any III-V ternary material and studying the V/III flux ratio dependence of the vapor-solid distributions.

ACKNOWLEDGMENT

VGD gratefully acknowledges financial support of the research grant of St. Petersburg State University (No. 93020138).

[1] M. B. Panish and M. Ilegams, *Progress in Solid State Chemistry* (Pergamon Press, New York, 1972), Vol. 7.

[2] S. Adachi, *Properties of Semiconductor Alloys: Group-IV, III–V and II–VI Semiconductors* (John Wiley & Sons, West Sussex, 2009).

[3] V. Tomashyk, *Ternary Alloys Based on III-V Semiconductors* (Taylor & Francis Group, Boca Raton, 2017).

[4] K. Kaiiyama, Vapor pressure dependence of the relative composition of III-V mixed crystals in vapor phase epitaxy, J. Electrochem. Soc. **123**, 423 (1976).

[5] B. W. Liang and C. W. Tu, A kinetic model for As and P incorporation behaviors in GaAsP grown by gas-source molecular beam epitaxy, J. Appl. Phys. **74**, 255 (1993).

[6] A. Y. Egorov, A. R. Kovsh, V. M. Ustinov, A. E. Zhukov, P. S. Kop'ev, and C. W. Tu, A thermodynamic analysis of the growth of III-V compounds with two volatile group V elements by molecular-beam epitaxy, J. Cryst. Growth **188**, 69 (1998).

[7] Y. Kumagai, J. Kikuchi, Y. Matsuo, Y. Kanagawa, K. Tanaka, and A. Koukitu, Thermodynamic analysis of InN and $In_xGa_{1-x}N$ MOVPE using various nitrogen sources, J. Cryst. Growth **272**, 341 (2004).

[8] Z. Ye, Y. Shu, X. Cao, L. Gong, B. Pi, J. Yao, X. Xing, and J. Xu, Thermodynamic analysis of growth of ternary III-V semiconductor materials by molecular-beam epitaxy, Trans. Nonferrous Met. Soc. China **21**, 146 (2011).

[9] S. N. G. Chu, S. Nakahara, K. E. Strege, and W. D. Johnston, Surface layer spinodal decomposition in $In_{1-x}Ga_xAs_yP_{1-y}$ and $In_{1-x}Ga_xAs$ grown by hydride transport vapor-phase epitaxy, J. Appl. Phys. **57**, 4610 (1985).

[10] Y. Kanagawa, T. Ito, Y. Kumagai, and A. Koukitu, Thermodynamic study on compositional instability of InGaN/GaN and InGaN/InN during MBE, Appl. Surf. Sci. **216**, 453 (2003).

[11] J. Adhikari and D. Kofke, Molecular simulation study of miscibility of ternary and quaternary InGaAlN alloys, J. Appl. Phys. **95**, 6129 (2004).

[12] B. Liu, J. Li, W. Yang, X. Zhang, X. Jiang, and Y. Bando, Semiconductor solid-solution nanostructures: Synthesis, property tailoring, and applications, Small **13**, 1701998 (2017).

[13] C.-Z. Ning, L. Dou, and P. Yang, Bandgap engineering in semiconductor alloy nanomaterials with widely tunable compositions, Nat. Rev. Mater. **2**, 17070 (2017).

[14] M. Heiss, A. Gustafsson, S. Conesa-Boj, F. Peiro, J. R. Morante, G. Abstreiter, J. Arbiol, L. Samuelson, and A. Fontcuberta i Morral, Catalyst-free nanowires with axial $In_xGa_{1-x}As$/GaAs heterostructures, Nanotechnology **20**, 075603 (2009).

[15] C. S. Jung, H. S. Kim, G. B. Jung, K. J. Gong, Y. I. Cho, S. Y. Jang, C. H. Kim, C. Lee, and J. Park, Composition and phase tuned InGaAs alloy nanowires, J. Phys. Chem. **115**, 7843 (2011).

[16] J. Wu, M. Borg, D. Jacobsson, K. A. Dick, and L. E. Wernersson, Control of composition and morphology in InGaAs nanowires grown by metalorganic vapor phase epitaxy, J. Cryst. Growth **383**, 158 (2013).

[17] G. Koblmüller and G. Abstreiter, Growth and properties of InGaAs nanowires on silicon, Phys. Stat. Solidi RRL **8**, 11 (2014).

[18] A. S. Ameruddin, H. A. Fonseka, P. Caroff, J. Wong-Leung, R. L. M. Op het Veld, J. L. Boland, M. B. Johnston, H. H. Tan, and C. Jagadish, $In_xGa_{1-x}As$ nanowires with uniform composition, pure wurtzite crystal phase and taper-free morphology, Nanotechnology **26**, 205604 (2015).

[19] A. S. Ameruddin, P. Caroff, H. H. Tan, C. Jagadish, and V. G. Dubrovskii, Understanding the growth and composition evolution of gold-seeded ternary InGaAs nanowires, Nanoscale **7**, 16266 (2015).

[20] V. G. Dubrovskii, I. V. Shtrom, R. R. Reznik, Yu. B. Samsonenko, A. I. Khrebtov, I. P. Soshnikov, S. Rouvimov, N. Akopian, T. Kasama, and G. E. Cirlin, Origin of spontaneous core-shell AlGaAs nanowires grown by molecular beam epitaxy, Cryst. Growth Des. **16**, 7251 (2016).

[21] P. K. Mohseni, A. Behnam, J. D. Wood, C. D. English, J. W. Lyding, E. Pop, and X. Li, $In_xGa_{1-x}As$ nanowire growth on graphene: Van der Waals epitaxy induced phase segregation, Nano Lett. **13**, 1153 (2013).

[22] S. Hertenberger, S. Funk, K. Vizbaras, A. Yadav, D. Rudolph, J. Becker, S. Bolte, M. Döblinger, M. Bichler, G. Scarpa *et al.*,

High compositional homogeneity in In-rich InGaAs nanowire arrays on nanoimprinted SiO_2/Si (111), Appl. Phys. Lett. **101**, 043116 (2012).
[23] G. Priante, G. Patriarche, F. Oehler, F. Glas, and J. C. Harmand, Abrupt GaP/GaAs interfaces in self-catalyzed nanowires, Nano Lett. **15**, 6036 (2015).
[24] G. Priante, F. Glas, G. Patriarche, K. Pantzas, F. Oehler, and J. C. Harmand, Sharpening the interfaces of axial heterostructures in self-catalyzed AlGaAs nanowires: Experiment and theory, Nano Lett. **16**, 1917 (2016).
[25] D. Jacobsson, J. M. Persson, D. Kriegner, T. Etzelstorfer, J. Wallentin, J. B. Wagner, J. Stangl, L. Samuelson, K. Deppert, and M. T. Borgstrom, Particle-assisted $Ga_xIn_{1-x}P$ nanowire growth for designed bandgap structures, Nanotechnology **23**, 245601 (2012).
[26] R. Yan, D. Gargas, and P. Yang, Nanowire photonics, Nat. Photonics **3**, 569 (2009).
[27] M. Zeghouane, G. Avit, Y. André, C. Bougerol, Y. Robin, P. Ferret, D. Castelluci, E. Gil, V. G. Dubrovskii, H. Amano, and A. Trassoudaine, Compositional control of homogeneous InGaN nanowires with the In content up to 90%, Nanotechnology **30**, 044001 (2019).
[28] G. Boras, X. Yu, and H. Liu, III-V ternary nanowires on Si substrates: Growth, characterization and device applications, J. Semicond. **40**, 101301 (2019).
[29] F. Martelli, III-V ternary nanowires, in *Advances in III-V Semiconductor Nanowires and Nanodevices*, edited by J. Li, D. Wang, and R. R. LaPierre (Bentham Science Publisher, Sharjah, 2011), pp. 105–128.
[30] A. Fakhr and Y. M. Haddara, Modelling of InGaP nanowires morphology and composition on molecular beam epitaxy growth conditions, J. Appl. Phys. **116**, 024314 (2014).
[31] V. G. Dubrovskii, Fully analytical description for the composition of ternary vapor-liquid-solid nanowires, Cryst. Growth Des. **15**, 5738 (2015).
[32] V. G. Dubrovskii, A. A. Koryakin, and N. V. Sibirev, Understanding the composition of ternary III-V nanowires and axial nanowire heterostructures in nucleation-limited regime, Mat. Design **132**, 400 (2017).
[33] J. Johansson and M. Ghasemi, The composition of gold alloy seeded InGaAs nanowires in the nucleation limited regime, Cryst. Growth Des. **17**, 1630 (2017).
[34] E. D. Leshchenko, M. Ghasemi, V. G. Dubrovskii, and J. Johansson, Nucleation-limited composition of ternary III-V nanowires forming from quaternary gold based liquid alloys, CrystEngComm **20**, 1649 (2018).
[35] J. Johansson and M. Ghasemi, Kinetically limited composition of ternary III-V nanowires, Phys. Rev. Mater. **1**, 040401(R) (2017).
[36] F. Glas, Comparison of modeling strategies for the growth of heterostructures in III–V nanowires, Cryst. Growth Des. **17**, 4785 (2017).
[37] E. D. Leshchenko and J. Johansson, Role of thermodynamics and kinetics in the composition of ternary III-V nanowires, Nanomaterials **10**, 2553 (2020).
[38] V. G. Dubrovskii, Understanding the vapor-liquid-solid growth and composition of ternary III-V nanowires and nanowire heterostructures, J. Phys. D: Appl. Phys. **50**, 453001 (2017).
[39] M. Ghasemi, E. D. Leshchenko, and J. Johansson, Assembling your nanowire: An overview of composition tuning in ternary III–V nanowires, Nanotechnology **32**, 072001 (2021).
[40] E. D. Leshchenko and V. G. Dubrovskii, Kinetic modeling of interfacial abruptness in axial nanowire heterostructures, Nanotechnology **34**, 065602 (2023).
[41] V. G. Dubrovskii and F. Glas, Vapor–liquid–solid growth of semiconductor nanowires, in *Fundamental Properties of Semiconductor Nanowires*, edited by N. Fukata and R. Rurali (Springer, Singapore, 2020).
[42] T. F. Kuech, III-V compound semiconductors: Growth and structures, Prog. Cryst. Growth Char. Mat. **62**, 352 (2016).
[43] J. R. Arthur, Molecular beam epitaxy, Surf. Sci. **500**, 189 (2002).
[44] A. V. Redkov and S. A. Kukushkin, Development of Burton–Cabrera–Frank theory for the growth of a non-Kossel crystal via chemical reaction, Cryst. Growth Des. **20**, 2590 (2020).
[45] J. Johansson, C. P. T. Svensson, T. Martensson, L. Samuelson, and W. Seifert, Mass transport model for semiconductor nanowire growth, J. Phys. Chem. B **109**, 13567 (2005).
[46] L. E. Fröberg, W. Seifert, and J. Johansson, Diameter-dependent growth rate of InAs nanowires, Phys. Rev. B **76**, 153401 (2007).
[47] G. E. Cirlin, V. G. Dubrovskii, N. V. Sibirev, I. P. Soshnikov, Yu. B. Samsonenko, A. A. Tonkikh, and V. M. Ustinov, The diffusion mechanism in the formation of GaAs and AlGaAs nanowhiskers during the process of molecular-beam epitaxy, Semiconductors **39**, 557 (2005).
[48] M. C. Plante and R. R. LaPierre, Analytical description of the metal-assisted growth of III–V nanowires: Axial and radial growths, J. Appl. Phys. **105**, 114304 (2009).
[49] J. C. Harmand, F. Glas, and G. Patriarche, Growth kinetics of a single $InP_{1-x}As_x$ nanowire, Phys. Rev. B **81**, 235436 (2010).
[50] V. G. Dubrovskii, Evolution of the length and radius of catalyst-free III-V nanowires grown by selective area epitaxy, ACS Omega **4**, 8400 (2019).
[51] F. Glas, M. R. Ramdani, G. Patriarche, and J. C. Harmand, Predictive modeling of self-catalyzed III-V nanowire growth, Phys. Rev. B **88**, 195304 (2013).
[52] V. G. Dubrovskii, T. Xu, A. Díaz Álvarez, G. Larrieu, S. R. Plissard, P. Caroff, F. Glas, and B. Grandidier, Self-equilibration of the diameter of Ga-catalyzed GaAs nanowires, Nano Lett. **15**, 5580 (2015).
[53] J. Tersoff, Stable self-catalyzed growth of III-V nanowires, Nano Lett. **15**, 6609 (2015).
[54] A. Pishchagin, F. Glas, G. Patriarche, A. Cattoni, J. C. Harmand, and F. Oehler, Dynamics of droplet consumption in vapor–liquid–solid III–V nanowire growth, Cryst. Growth Des. **21**, 4647 (2021).
[55] V. G. Dubrovskii, *Nucleation Theory and Growth of Nanostructures* (Springer, Heidelberg, 2014).
[56] W. K. Burton, N. Cabrera, and F. C. Frank, The growth of crystals and the equilibrium structure of their surfaces, Philos. Trans. A Math Phys. Eng. Sci. **243**, 299 (1951).
[57] P. Aseev, A. Fursina, F. Boekhout, F. Krizek, J. E. Sestoft, F. Borsoi, S. Heedt, G. Wang, L. Binci, S. Martí-Sánchez *et al.*, Selectivity map for molecular beam epitaxy of advanced III-V quantum nanowire networks, Nano Lett. **19**, 218 (2019).
[58] D. Dede, F. Glas, V. Piazza, N. Morgan, M. Friedl, L. Guniat, E. Nur Dayi, A. Balgarkashi, V. G. Dubrovski, and A. Fontcuberta i Morral, Selective area epitaxy of GaAs: The unintuitive role of feature size and pitch, Nanotechnology **33**, 485604 (2022).

[59] V. G. Dubrovskii, Theory of diffusion-induced selective area growth of III-V nanostructures, Phys. Rev. Mater. **7**, 026001 (2023).
[60] J. A. Rogers, M. G. Lagally, and R. G. Nuzzo, Synthesis, assembly and applications of semiconductor nanomembranes, Nature (London) **477**, 45 (2011).
[61] X. Yuan, D. Pan, Y. Zhou, X. Zhang, K. Peng, B. Zhao, M. Deng, J. He, J. H. H. Tan, and C. Jagadish, Selective area epitaxy of III–V nanostructure arrays and networks: Growth, applications, and future directions, Appl. Phys. Rev. **8**, 021302 (2021).
[62] J. Yoon, III-V nanomembranes for high performance, cost-competitive photovoltaics, MRS Adv. **2**, 1591 (2017).
[63] C.-Y. Chi, C.-C. Chang, S. Hu, T.-W. Yeh, S. B. Cronin, and P. D. Dapkus, Twin-free GaAs nanosheets by selective area growth: Implications for defect-free nanostructures, Nano Lett. **13**, 2506 (2013).
[64] G. Tutuncuoglu, M. de la Mata, D. Deiana, H. Potts, F. Matteini, J. Arbiol, and A. Fontcuberta i Morral, Towards defect-free 1-D GaAs/AlGaAs heterostructures based on GaAs nanomembranes, Nanoscale **7**, 19453 (2015).
[65] P. Hanggi, P. Talkner, and M. Borkovec, Reaction-rate theory: Fifty years after Kramers, Rev. Mod. Phys. **62**, 251 (1990).
[66] V. G. Dubrovskii and Yu. Yu. Hervieu, Diffusion-induced growth of nanowires: Generalized boundary conditions and self-consistent kinetic equation, J. Cryst. Growth **401**, 431 (2014).
[67] F. Glas, Chemical potentials for Au-assisted vapor-liquid-solid growth of III-V nanowires, J. Appl. Phys. **108**, 073506 (2010).
[68] J. Johansson and M. H. Magnusson, From diffusion limited to incorporation limited growth of nanowires, J. Cryst. Growth **525**, 125192 (2019).
[69] V. G. Dubrovskii, Group V sensitive vapor-liquid-solid growth of Au-catalyzed and self-catalyzed III-V nanowires, J. Cryst. Growth **440**, 62 (2016).
[70] D. Kashchiev, Dependence of the growth rate of nanowires on the nanowire diameter, Cryst. Growth Des. **6**, 1154 (2006).
[71] V. G. Dubrovskii, N. V. Sibirev, G. E. Cirlin, A. D. Bouravleuv, Yu. B. Samsonenko, D. L. Dheeraj, H. L. Zhou, C. Sartel, J. C. Harmand, G. Patriarche *et al.*, Role of non-linear effects in nanowire growth and crystal phase, Phys. Rev. B **80**, 205305 (2009).
[72] F. Glas, Vapor fluxes on the apical droplet during nanowire growth by molecular beam epitaxy, Phys. Stat. Solidi B **247**, 254 (2010).
[73] R. Sjökvist, D. Jacobsson, M. Tornberg, R. Wallenberg, E. D. Leshchenko, J. Johansson, and K. A. Dick, Compositional correlation between the nanoparticle and the growing Au-assisted $In_xGa_{1-x}As$ nanowire, J. Phys. Chem. Lett. **12**, 7590 (2021).
[74] I. Ansara, C. Chatillon, H. L. Lukas, T. Nishizawa, H. Ohtani, K. Ishida, M. Hillert, B. Sundman, B. B. Argent, A. Watson *et al.*, A binary database for III–V compound semiconductor systems, Calphad **18**, 177 (1994).
[75] A. T. Dinsdale, SGTE unary database ver. 4.4, Calphad **15**, 317 (1991).
[76] J.-Y. Shen, C. Chatillon, I. Ansara, A. Watson, B. Rugg, and T. Chart, Optimisation of the thermodynamic and phase diagram data in the ternary As-Ga-In system, Calphad **19**, 215 (1995).
[77] C. Li, J. B. Li, Z. Du, and W. Zhang, A thermodynamic assessment of the Ga-In-P system, J. Phase Equil. **21**, 357 (2000).
[78] See Supplemental Material at http://link.aps.org/supplemental/10.1103/PhysRevMaterials.7.056001 for thermodynamic parameters of InGaAs and InGaP material systems.
[79] D. McLean, *Grain Boundaries in Metals* (Oxford University Press, New York, 1957).
[80] H. Durmaz, P. Sookchoo, X. Cui, R. B. Jacobson, D. E. Savage, M. G. Lagally, and R. Paiella, SiGe nanomembrane quantum-well infrared photodetectors, ACS Photonics **3**, 1978 (2016).
[81] P. Tomasini, Mapping vapor–solid distributions of silicon germanium chemical vapor depositions, J. Cryst. Growth **563**, 126106 (2021).
[82] M. Borg, J. Johansson, K. Storm, and K. Deppert, Geometric model for metalorganic vapour phase epitaxy of dense nanowire arrays, J. Cryst. Growth **366**, 15 (2013).
[83] V. V. Fedorov, L. N. Dvoretckaia, D. A. Kirilenko, I. S. Mukhin, and V. G. Dubrovskii, Formation of wurtzite sections in self-catalyzed GaP nanowires by droplet consumption, Nanotechnology **32**, 495601 (2021).